Toward Exploring the Synergy Between Cloud Radar Polarimetry and Doppler Spectral Analysis in Deep Cold Precipitating Systems in the Arctic

Mariko Oue[1] [ID]**, Pavlos Kollias[1,2]** [ID]**, Alexander Ryzhkov[3], and Edward P. Luke[2]**

[1]School of Marine and Atmospheric Sciences, Stony Brook University, Stony Brook, NY, USA, [2]Environmental and Climate Sciences Department, Brookhaven National Laboratory, Upton, NY, USA, [3]Cooperative Institute for Mesoscale Meteorological Studies/National Severe Storms Laboratory, Moss Landing, CA, USA

Abstract The study of Arctic ice and mixed-phase clouds, which are characterized by a variety of ice particle types in the same cloudy volume, is challenging research. This study illustrates a new approach to qualitative and quantitative analysis of the complexity of ice and mixed-phase microphysical processes in Arctic deep precipitating systems using the combination of Ka-band zenith-pointing radar Doppler spectra and quasi-vertical profiles of polarimetric radar variables measured by a Ka/W-band scanning radar. The results illustrate the frequent occurrence of multimodal Doppler spectra in the dendritic/planar growth layer, where locally generated, slower-falling particle populations are well separated from faster-falling populations in terms of Doppler velocity. The slower-falling particle populations contribute to an increase of differential reflectivity (Z_{DR}), while an enhanced specific differential phase (K_{DP}) in this dendritic growth temperature range is caused by both the slower and faster-falling particle populations. Another area with frequent occurrence of multimodal Doppler spectra is in mixed-phase layers, where both populations produce Z_{DR} and K_{DP} values close to 0, suggesting the occurrence of a riming process. Joint analysis of the Doppler spectra and the polarimetric radar variables provides important insight into the microphysics of snow formation and allows the separation of the contributions of ice of different habits to the values of reflectivity and Z_{DR}.

1. Introduction

Ice microphysical processes have dependencies on temperature, relative humidity, amount of cloud water present, aerosol loading, precipitation, and cloud dynamics (Khain et al., 2015). These processes interact and drive the complexities of ice microphysics, particularly in the Arctic. One of the phenomena specific to the Arctic is the frequent presence of mixed-phase clouds (Karlsson & Svensson, 2011; Lebo et al., 2008; Tan et al., 2016), which are defined as clouds in which supercooled liquid water droplets and solid ice crystals coexist at temperatures between −40°C and 0°C. These mixed-phase clouds occur as persistent single or multiple stratiform layers embedded in Arctic precipitating and nonprecipitating systems (Morrison et al., 2012; Shupe, 2011), which can produce a variety of ice particle types in the same volume of a cloud. Understanding ice microphysical processes in the Arctic is a challenge due to these complex interactions. The complex microphysical processes make them difficult to accurately characterize from an observational viewpoint, and, thus, even more difficult to parameterize in models.

Aircraft-based in situ measurements are the most reliable observational platform for studying complex microphysical and dynamical processes of Arctic clouds; however, such observations are difficult to routinely perform in the Arctic (Korolev et al., 2003). Collocated observations by millimeter-wavelength radars and polarization lidars have been used from space (e.g., Cesana et al., 2012; Zhang et al., 2010) and the ground (Shupe et al., 2008) to identify the presence of embedded supercooled liquid layers in mixed-phase clouds by exploiting the sensitivity of lidars to the numerous liquid droplets and the sensitivity of radars to the fewer but larger ice particles.

Advancing beyond the identification of mixed-phase clouds requires the use of multiparameter radar observations such as those based on Doppler spectra, polarimetry, and multiple wavelengths. Doppler spectra measured by profiling millimeter-wavelength radars offer the ability to identify and separate the contributions of liquid and ice hydrometeors to the radar returns and perform microphysical and dynamical retrievals (Kalesse et al., 2016; Luke et al., 2010; Shupe et al., 2004; Verlinde et al., 2013). Observations at

different radar wavelengths utilize the frequency-dependent attenuation and backscattering properties of hydrometeors (Kneifel et al., 2015, 2016; Leinonen & Moisseev, 2015; Tridon et al., 2013). In addition to radar Doppler spectra and multiwavelength measurements, radar polarimetry can also offer unique insights into ice/snow particle properties. Polarimetric observables from cloud and precipitation radars offer the capability to identify ice hydrometeor species such as pristine ice crystals, aggregates, graupel, and ice pellets (e.g., Hall et al., 1984; Matrosov, 1991; Straka & Zrnić, 1993; Reinking et al., 1997) as well as their spatial distributions (e.g., Andrić et al., 2013; Kumjian et al., 2013; Schneebeli et al., 2013; Thompson et al., 2014). Polarimetric cloud radars operating at shorter wavelengths are more sensitive to the presence of smaller ice particles (e.g., Matrosov et al., 2017) and liquid cloud droplets (Myagkov et al., 2016). Differential reflectivity (Z_{DR}) and specific differential phase (K_{DP}) depend on the size, aspect ratio, bulk density, and orientation of particles, while K_{DP} is also proportional to the number concentration (e.g., Ryzhkov et al., 1998).

It is very common for different habits of ice particles to coexist in the radar resolution volume and it is impossible to separate and quantify their relative amounts if a single radar variable such as radar reflectivity (Z_H) is utilized. The mixture of different habits of ice particles is often the case in the dendritic/planar crystal growth layer (DGL) within the temperature interval from −20 to −10°C where quasi-spherical ice with irregular shape produced near the top of the cloud is mixed with locally generated anisotropic ice in the form of dendrites and/or hexagonal plates (e.g., Kennedy & Rutledge, 2011). Another notable layer where aggregated or rimed snow coexists with highly anisotropic small needle-like crystals is often found at warmer temperatures where the Hallett-Mossop ice multiplication process (−8 to −3°C, Hallett & Mossop, 1974) is active. Various ice habits contribute differently to Z_H, Z_{DR}, and K_{DP}, and some segregation of different ice types within the radar resolution volume is possible when all three radar variables are analyzed. Schrom et al. (2015) suggested a polarimetric technique to separate contributions from aggregates and dendrites in the DGL of midlatitude winter storms. Polarimetric signatures of the secondary ice mixed with aggregated and rimed snow in layers with temperature around −5°C were found by cloud and precipitation radar measurements in high-latitude deeper snow clouds (Oue, Kumjian, Lu, Verlinde, et al., 2015; Sinclair et al., 2016), midlatitude mesoscale convective systems (Giangrande, Toto, Bansemer, et al., 2016; Kumjian et al., 2016), and midlatitude snowstorms (Kumjian & Lombardo, 2017). However, combining polarimetric measurements with the analysis of Doppler spectra yields a much better chance to identify and separate different types of ice, and to quantify their amounts if their corresponding fall velocities are associated with separate peaks in the Doppler spectrum. As an example, Moisseev et al. (2015) linked the onset of snow particle growth via aggregation, manifested by bimodal Doppler spectra, to enhancement of K_{DP} values and suggested that the K_{DP} enhancement required high number concentrations of oblate ice particles produced in the ice multiplication regions.

Several previous studies have analyzed polarimetric signatures in ice regions observed in midlatitude heavy-snow-producing winter storms by longer-wavelength precipitation radars operating at S and C bands (e.g., Andrić et al., 2013; Kennedy & Rutledge, 2011; Kumjian et al., 2014; Williams et al., 2015). However, polarimetric radar analysis of Arctic clouds faces the challenge of lower ice water content and smaller ice particles compared to midlatitude storms, resulting in low signal-to-noise ratio (SNR) and weak K_{DP} signatures at longer radar wavelengths (Oue et al., 2016). Rather than heavy riming, light riming likely occurs most often in the Arctic region because of relatively weak upward velocities (e.g., Lawson & Zuidema, 2009; Shupe et al., 2008) and/or low concentrations of liquid cloud droplets and, therefore, low liquid water content (Jayaweera & Ohtake, 1973). Verlinde et al. (2013) reported that small graupel can be produced when deep frontal ice-precipitating clouds contain supercooled liquid cloud layers. Light riming and production of small graupel would be difficult to distinguish from aggregation processes using vertical gradients of reflectivity and vertical velocity as described in Oue et al. (2016) and Schrom and Kumjian (2016).

The U.S. Department of Energy Atmospheric Radiation Measurement (ARM) program operates an atmospheric observatory at Oliktok Point, Alaska (Mather & Voyles, 2013), where profiling and scanning millimeter-wavelength cloud radars provide unique multiwavelength, polarimetric, and Doppler spectral measurements (Kollias et al., 2007, 2014). Herein, the benefit of combining height-versus-time fields of polarimetric radar variables and Doppler spectra is demonstrated in two key areas of the clouds where different ice particle types and cloud water may coexist: the DGL and the mixed-phase layer (MPL) beneath.
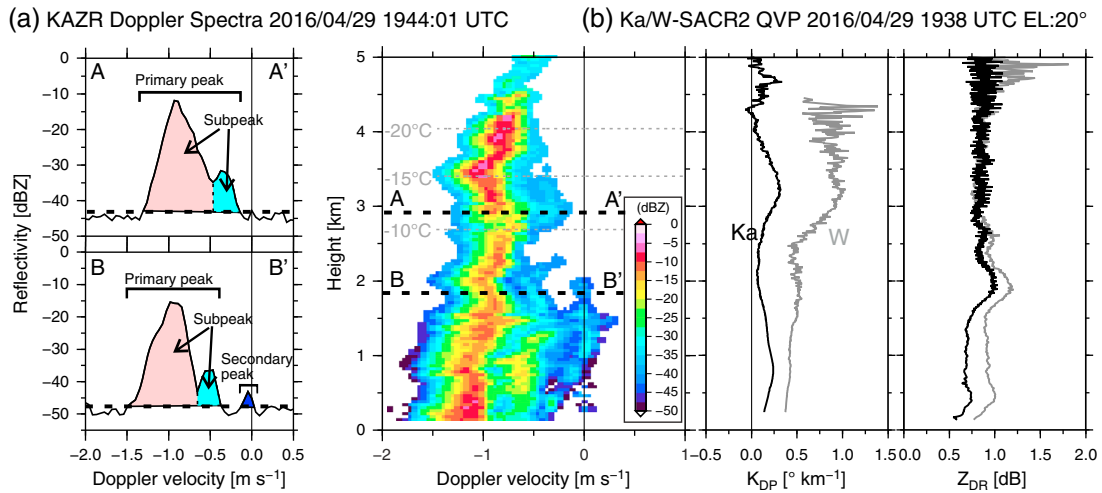
Figure 1. (a) Example of Ka-band ARM Zenith pointing Radar Doppler velocity spectra showing a profile and single spectrum along A-A′ and B-B′. Color shade in the profile plot represents reflectivity. Horizontal gray dashed lines represent heights of temperature of $-10°C$, $-15°C$, and $-20°C$. (b) Quasi-vertical profiles (QVPs) of K_{DP} and Z_{DR} estimated from a Ka (black lines) and W (gray lines) SACR2 PPI scan at an elevation angle of 20°.

2. Data and Method

Data were collected by the ARM Mobile Facility at the Oliktok site instrumented with a Ka-band ARM Zenith pointing Radar (KAZR, Kollias et al., 2016), Ka- and W-band second-generation Scanning ARM Cloud Radars (Ka/W-SACR2), ceilometer, microwave radiometer (MWR), Multi-Angle Snowflake Camera (MASC, Garrett et al., 2015), and sounding equipment (ARM Climate Research Facility, 2013a, 2013b, 2013c, 2016a, 2016b) in the spring season in 2016. We used liquid water path (LWP) retrieved from radiometric measurements (ARM Climate Research Facility, 2013b) using the statistical method developed by Liljegren et al. (2001). Sounding measurements were made at 0000 UTC and 1800 UTC every day, and we used those at a nearest time in each plot in this study.

2.1. KAZR MicroARSCL

During the observation period of this study, KAZR collected 256-point Doppler spectra with a temporal resolution of 2 s. The Nyquist velocity of the Doppler spectrum is 5.98 m s^{-1}, resulting in the velocity resolution of 0.047 m s^{-1}. The range spacing of the KAZR is 30 m, and the beam width is 0.33°. The recorded radar Doppler spectra are postprocessed to generate the Microscale Active Remote Sensing of Clouds (MicroARSCL; Kollias et al., 2007; Luke et al., 2008) data product via objective analysis of the Doppler spectrum morphology for estimating a number of its shape parameters. Of particular interest to this study is the detection of multipeak Doppler spectra, the decomposition of the Doppler spectrum into a primary peak and a secondary peak, and the estimation of the radar reflectivity and mean Doppler velocity separately for each peak. The primary peak is also decomposed into subpeaks, the edges of which are defined to be at local minima of power (Figure 1a), and the reflectivity and mean Doppler velocity of which are calculated. The definition of these peaks is illustrated in Figure 1a and described in section 2.3.

2.2. Ka/W-SACR2 Observations

The Ka/W-SACR2 radars perform polarimetric measurements through alternate transmission of horizontally (H) and vertically (V) polarized waves and simultaneous reception of copolar and cross-polar components of the backscattered wave. Therefore, a full set of polarimetric radar observables is available including Z_H, Z_{DR}, differential phase (φ_{DP}), copolar correlation coefficient (ρ_{hv}), linear depolarization ratio, along with Doppler velocity, spectral width, and dual-wavelength ratio (DWR) of Ka-band reflectivity and W-band reflectivity. The Ka-band and W-band radars share the same pedestal and have different size antennas to ensure a matched beam width (0.32°) at the two radar wavelengths. The range gate spacing for both radars is 30 m.

The Ka/W-SACR2 observed reflectivity is corrected for gaseous attenuation based on sounding measurements at 1800 UTC for each day using a methodology proposed by Liebe et al. (1993). The Ka/W-SACR2

Z_{DR} measurements are corrected for systematic biases (Seliga et al., 1981) by averaging Z_{DR} from zenith-pointing 360° rotation scans and found to be equal to 0.11 dB for Ka-SACR2 and −0.62 dB for W-SACR2. Additional biases attributed to elevation dependencies of Z_{DR} and K_{DP} are corrected using theoretical formulas presented in Ryzhkov et al. (2005) and Schneebeli et al. (2013). The Z_{DR} values at range gates with sufficiently high SNR (>0 dB) have been used in our analysis.

Specific differential phase K_{DP} was estimated using an iterative algorithm proposed by Hubbert and Bringi (1995). The algorithm starts with radial smoothing of the measured profile of total differential phase φ_{DP} and retaining of the φ_{DP} values where $\rho_{hv} > 0.8$ and SNR > 3 dB. If the difference between the filtered (smoothed) and raw φ_{DP} values is greater than 5°, then the filtered φ_{DP} value is subsequently used in a new iteration to obtain an updated φ_{DP} profile. K_{DP} is then computed as a slope of the smoothed φ_{DP} profile divided by 2. The slope is estimated as a linear least square fit applied to 66 Ka/W-SACR2 radar range gates over 2 km of radial distance. This method eliminates most of the backscatter differential phase effects (if any) in cold parts of cloud above the melting layer.

This study utilizes the quasi-vertical profile (QVP) methodology (Kumjian & Lombardo, 2017; Ryzhkov et al., 2016) using SACR2 higher-elevation plan position indicator (PPI) scans. The QVP technique employs azimuthal averaging of polarimetric radar variables from conical PPI scans at high elevations (6.4° to 28°) to produce QVPs of polarimetric radar variables in a height versus time format. The QVPs have high vertical resolution allowing the capture of important polarimetric radar signatures and their evolution (e.g., Griffin et al., 2017; Kumjian & Lombardo, 2017). We use PPI scans at an elevation angle of 20° every 30 min with a scan rate of $2°\ s^{-1}$. Since the slant range resolution of the PPI data is 30 m, the corresponding vertical spacing of the QVP data is about 10 m. Note that the actual vertical resolution of QVP is determined by the vertical size of the radar resolution volume, which increases with distance from the radar (Ryzhkov et al., 2016). The use of high elevation angle for QVP reconstruction (20°) ensures relatively high horizontal resolution at lower altitudes (11 km at the height of 2 km) that facilitates direct comparison with the KAZR Doppler spectra profiles. The KAZR data were vertically interpolated to the QVP height grid to match the QVP and KAZR data. Because a single PPI scan takes 3 min at the antenna rotation rate of $2°\ s^{-1}$, every SACR2 PPI corresponds to about 90 profiles of the KAZR MicroARSCL data.

2.3. Synergetic Analysis

Because radar Doppler velocities are related to particle fall speeds and vertical air motions, multimodality of the Doppler spectra indicates different particle populations coexisting in the radar sampling volume. The multimodal radar Doppler spectra have often been used to infer the presence of mixed-phase conditions in deep precipitating ice clouds (e.g., Luke et al., 2010; Oue, Kumjian, Lu, Verlinde, et al., 2015, Oue, Kumjian, Lu, Jiang, et al., 2015). An example of multimodal spectra is shown in Figure 1a. In ice precipitation clouds, total reflectivity is dominated by ice particles, which is shown as a primary peak in the Doppler spectrum (A-A′). We assume that the primary peak may contain a maximum of two subpeaks: the one associated with faster-falling particles which generally produce higher reflectivity (called the fast-falling subpeak hereafter) and the one attributed to slower-falling particles with lower reflectivity (called the slow-falling subpeak hereafter), implying that faster-falling particles have larger sizes and/or higher concentrations. Although the fast-falling subpeak can produce weaker reflectivity when the particle number concentration is very low, this was not common during the spring season at the Oliktok site. Slow-falling subpeaks generally have mean Doppler velocity $< -0.3\ m\ s^{-1}$, suggesting falling ice particles rather than liquid ones. Doppler spectra of cloud droplets commonly have mean Doppler velocity either near $0\ m\ s^{-1}$ or slightly positive (Rambukkange et al., 2011). When a slow-falling subpeak produces nearly $0\ m\ s^{-1}$ mean Doppler velocity and low reflectivity (<−20 dBZ), the corresponding particles are likely liquid cloud droplets (Yu et al., 2014). Often, the cloud droplet Doppler spectrum is clearly separated from the ice spectrum (B-B′, Figure 1a). The ceilometer cloud base is an indicator of the presence of cloud droplets, but the ceilometer beam cannot penetrate the low level liquid cloud to reach potential further liquid layers at higher altitudes. The Doppler spectra measurements, on the other hand, can capture the upper cloud layers.

The QVPs of Ka/W-SACR2 K_{DP} and Z_{DR} corresponding to the KAZR Doppler spectra in Figure 1a are shown in Figure 1b. K_{DP} at both frequencies starts to increase at around 4 km altitude until attaining maximum values
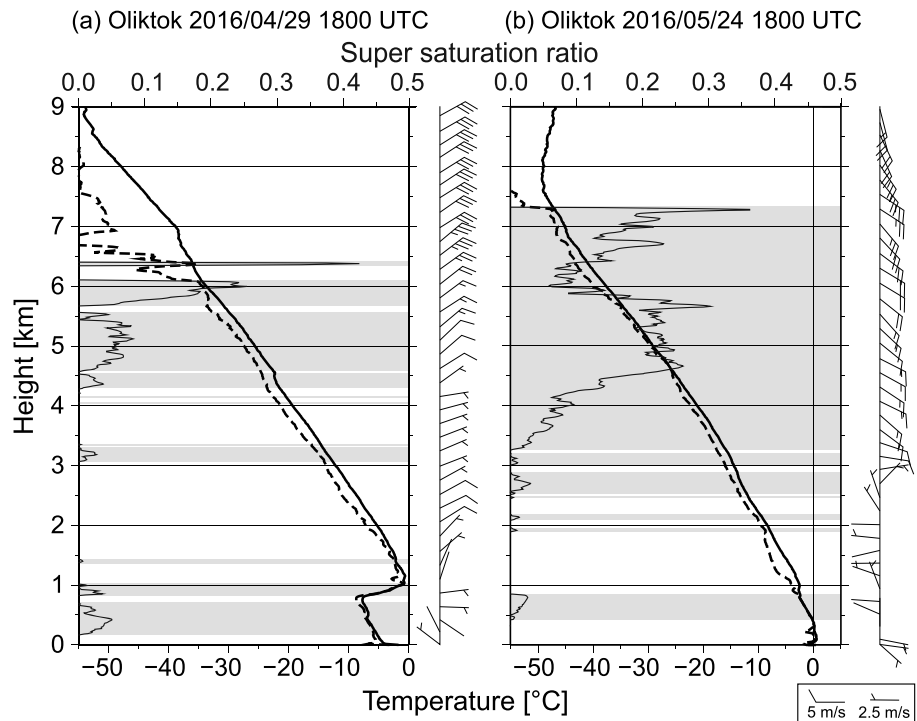
Figure 2. Temperature (thick solid line), dew point temperature (dashed line), supersaturation ratio with respect to ice (thin line), and horizontal wind (barb) profiles from sounding measurements at Oliktok at 1800 UTC on (a) 29 April 2016 and (b) 24 May 2016. Shaded regions represent supersaturation conditions with respect to ice.

at around 3.2 km and then decreases until around 2.5 km altitude. The corresponding temperature range of this layer is from −20 to −10°C, favoring the growth of dendrites and plates (Magono & Lee, 1966; Pruppacher & Klett, 2010). In the altitude range of the K_{DP} enhancement, the KAZR Doppler spectra show multimodality (2.7–3.6 km), while Z_{DR} is relatively low. The low Z_{DR} values can be attributed to large, more isotropic (quasi-isotropic) ice particles which dominate the total reflectivity. The higher K_{DP} values can be attributed to anisotropic particles and slower-falling oblate particles. Quasi-isotropic particles, which still have aspect ratios less than 1, can also produce enhanced K_{DP} if their concentration is sufficiently high. The lack of correlation between K_{DP} and Z_{DR} has been commonly observed in the data collected by shorter-wavelength radars and suggests that small oblate particles and larger aggregates are mixed in the same radar sampling volume (e.g., Schrom et al., 2015; Oue, Kumjian, Lu, Jiang, et al., 2015).

3. Results

Two deep precipitating ice events observed by the KAZR and the Ka/W-SACR2 on 29 April and 24 May 2016 are analyzed in this study. Temperature and wind profiles from sounding measurements at 1800 UTC for the two cases are shown in Figure 2. The time-height structure of the radar reflectivity and mean Doppler velocity of the KAZR Doppler spectra primary peak for the two cases is illustrated in Figures 3a and 3b, respectively, with temperature data overlaid (horizontal dashed lines). The ceilometer cloud base detections are also shown, indicating the presence of supercooled liquid droplet layers if the temperatures at the cloud bases are subfreezing. Both ice precipitation cases were associated with deep cloud systems with cloud tops reaching 7.5 km altitude in the early period of each of the two events. For the 29 April case, the cloud top heights descend to 5.5 km altitude until 1800 UTC, while the cloud top temperatures increase from −45 to −30°C. The cloud top heights vary between 4.5 and 5.5 km after 1800 UTC until 2300 UTC. Temperatures are below freezing through the cloud depth, and there is an inversion layer at 1 km altitude. Horizontal wind speeds are generally lower than 8 m s^{-1} within the cloud. For the 24 May case, the cloud top is at 7.5 km until 2000 UTC and then decreases to 5 km until 2200 UTC, while cloud top temperatures increase from −50 to −30°C. Horizontal
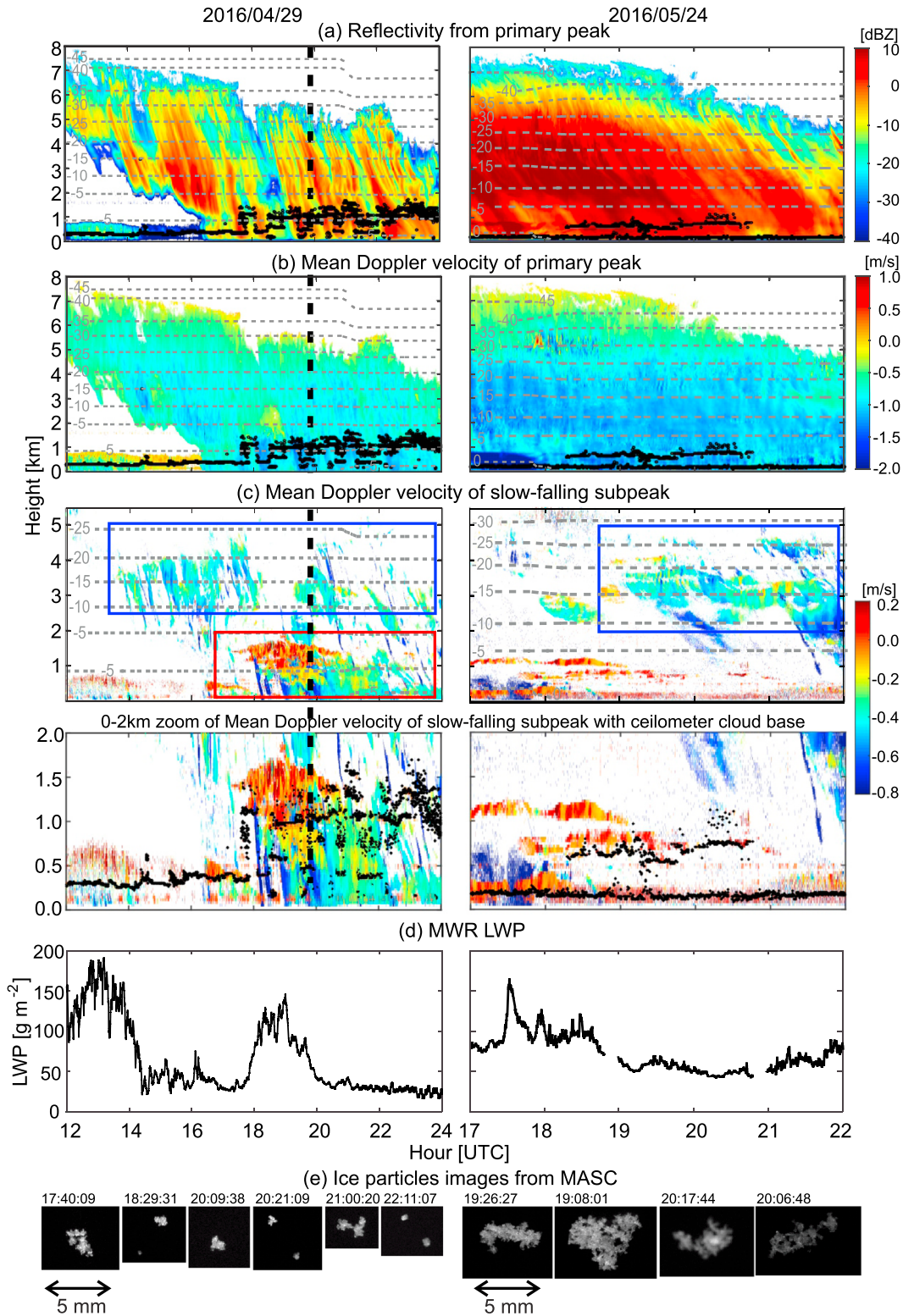
Figure 3. Height versus time cross sections of (a) Ka-band ARM Zenith pointing Radar (KAZR) reflectivity, (b) KAZR mean Doppler velocity, and (c) mean Doppler velocity of slow-falling subpeaks, (d) microwave radiometer (MWR)-retrieved liquid water path (LWP), and (e) images of ice particles recorded by the MASC at the ground for 29 April 2016 (left column) and 24 May 2016 (right column). Boxes in (c) represent the dendritic/planar growth layers (blue) and the mixed-phase layer (red) analyzed in this study. Black dots in (a), (b), and zoomed plots in (c) represent ceilometer-observed cloud base heights indicating the presence of liquid droplet layers. Gray dashed lines in (a–c) represent temperature with a 5 K increment from soundings at Oliktok. MASC = Multi-Angle Snowflake Camera.

wind speed is 10–12 m s^{-1} above 5.5 km and <8 m s^{-1} below 5.5 km altitude with pronounced vertical wind shear at 3 km.

The mean Doppler velocity of the slow-falling subpeak within the primary Doppler spectrum peak is shown in Figure 3c along with MWR-retrieved LWP in Figure 3d and samples of ice particle images from the MASC in Figure 3e. In the 29 April case, many of the recorded radar Doppler spectra exhibit slower-falling subpeaks within a 2.5–5 km height range with temperature varying from −25 to −8°C. This layer includes regions of supersaturation with respect to ice (Figure 2a) favorable to hexagonal plate crystal growth and dendritic growth (if enough water vapor is present). We selected the layer from 2.5 to 5 km at 1315–2348 UTC and defined it as the DGL of this case in this study (blue box in Figure 3c). Although the plate-like crystal growth layer, and especially the dendritic growth layer, can be narrower than the selected layer, these crystals can be present with warmer temperatures than the growth temperature range as they fall with an absence of aggregation (e.g., Griffin et al., 2017; Matrosov et al., 2017). The time range was determined on the basis of the QVP times. The slow-falling subpeaks have a significant downward value of Doppler velocity (0.3–0.8 m s^{-1}) suggesting slowly falling ice rather than supercooled cloud droplets. Below 2 km height, where observed temperatures vary from −8 to −1°C, slower-falling ice subpeaks are observed as extensive horizontal layers. In this layer (below 2 km), the slower-falling subpeaks have Doppler velocities around 0 m s^{-1} indicating the presence of supercooled liquid droplets. This is further supported by the ceilometer-detected cloud bases (Figures 3a and 3b) and increase in MWR LWP (Figure 3d). The MASC observed compact, rimed particles at the ground (Figure 3e), suggesting that ice particles fell through supercooled liquid cloud layers. We selected this layer (below 2 km between 1645 and 2348 UTC, red box in Figure 3c) for the analysis and defined it as a mixed-phase layer or MPL.

Slow-falling subpeaks with an ice signature (Doppler velocity 0.3–1.0 m s^{-1}) are also shown in the 24 May case from 1800 UTC to 2200 UTC at altitudes with temperature ranging from −30 to −5°C including regions of supersaturation with respect to ice and the DGL centered at −15°C (Figure 2b). KAZR reflectivity and mean Doppler velocity indicate signatures of melting layer and rain below 0.9 km altitude shown as a reflectivity bright band (Figure 3a) and a large increase in the magnitude of mean Doppler velocity (Figure 3c) before around 1800 UTC. To avoid including KAZR and Ka/W-SACR2 data with significant attenuation due to rain in our analysis, we selected an analysis period from 1845 UTC to 2148 UTC and altitude 1.5–5 km (temperature range from −8 to −29°C, defined as the DGL of the 24 May case, blue box in Figure 3c). Below 1.1 km, subpeaks with Doppler velocities around 0.0 m s^{-1} or positive values are observed. The ceilometer-observed cloud bases are also shown at ~0.8 km altitude and near the ground, while the MWR showed LWP between 40 and 90 g m^{-2} (Figure 3e), suggesting the presence of liquid cloud droplets in this layer. From the sounding profile at 1800 UTC on 24 May 2016 (Figure 2b), the slow-falling subpeaks and ceilometer cloud base around 1 km altitude seem to be supercooled liquid signatures, but those near the ground are likely attributed to melting snow and/or rain. Indeed, the slow-falling subpeak Doppler velocity was less than −1.5 m s^{-1} below 0.8 km altitude at 1700–1800 UTC. After 1800 UTC, there are little signatures of slowly falling ice subpeaks below 1 km altitude. In this study, we focus on the multimodality of ice particle Doppler spectra and therefore exclude this layer from consideration. The MASC observed aggregates of dendrites with little riming. In the rest of this section, emphasis is given to the DGL (for both cases, blue boxes in Figure 3c) and MPL (for the 29 April case, red box in Figure 3c).

3.1. Dendritic/Planar Growth Layer

The probability density distributions of radar reflectivity versus mean Doppler velocity for the fast- and slow-falling Doppler spectra subpeaks in the two DGLs are shown in Figures 4a–4d. The gradient of the mean Doppler velocity (V) with radar reflectivity (Z), dV/dZ, can be a useful parameter for identifying different growth processes such as riming or aggregation/deposition (e.g., Kalesse et al., 2013; Orr & Kropfli, 1999; Protat & Williams, 2011; Straka et al., 2000).

In the plots shown in Figure 4, vertical air motions were not considered. The Doppler spectra of the subpeaks of the primary peak and the secondary peaks included velocity values slightly departing from 0.0 m s^{-1} in the range from −0.3 to 0.2 m s^{-1} in the MPL, suggesting a presence of vertical air motion. The vertical air motion can produce uncertainties in the particle fall speed analysis. The gradient dV/dZ is shown in each plot together with the coefficient of determination (R^2) for the linear fitting. The R^2 values in the DGLs are
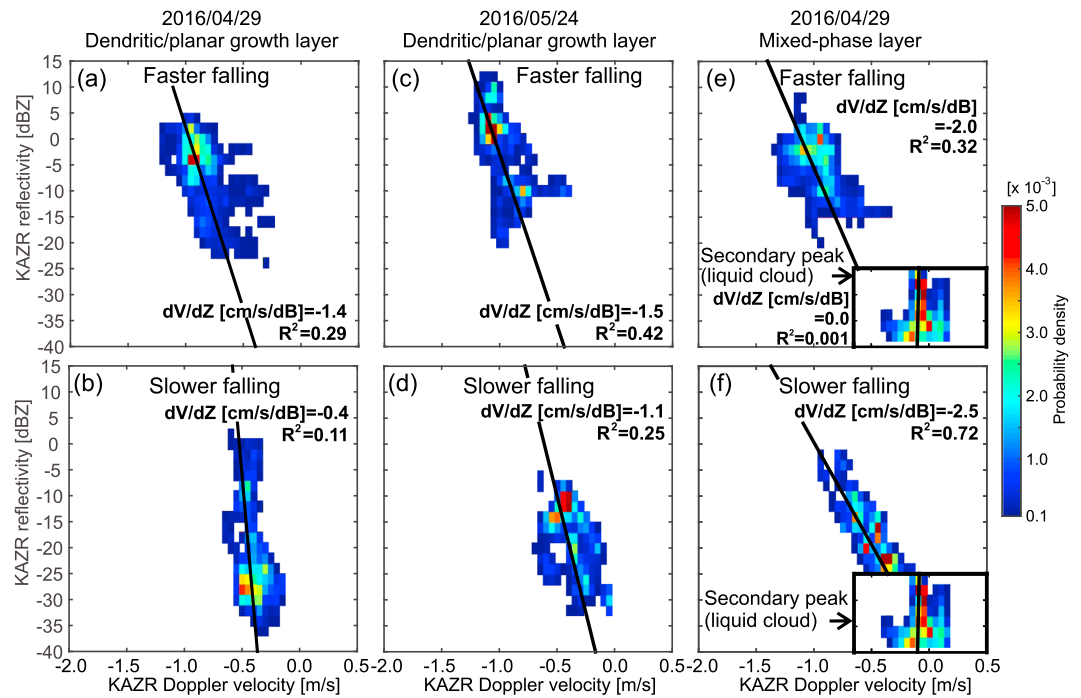
Figure 4. Probability density distributions of Ka-band ARM Zenith pointing Radar (KAZR) reflectivity versus KAZR Doppler velocity for the fast-falling subpeaks (a, c, and e) and slow-falling subpeaks (b, d, and f) for (a and b) the dendritic/planar crystal growth layer of 29 April (blue box in Figure 3c, left column), (c and d) for the dendritic/planar crystal growth layer of 24 May 2106 (blue box in Figure 3c, right column), and (e and f) the mixed-phase layer of 29 April 2016 (red box in Figure 3c, left column). The linear least squares fitting lines, their slopes (dV/dZ), and the coefficients of determination (R^2) are presented in each panel. Same but from the secondary peaks for the 29 April mixed-phased layer is inset in (e) and (f).

relatively low (fast-falling and slow-falling subpeaks of the 29 April case and slow-falling subpeaks of the 24 May case). The uncertainty could be associated with individual particle properties such as particle density, shape, and particle orientation, in addition to vertical air motions. Although each particle's fall speed can be affected by these factors, the reflectivity-Doppler velocity plots for each subpeak show differences in gradient dV/dZ values which are likely attributable to the different particle types and growth.

The downward velocity increases with reflectivity in both fast-falling and slow-falling subpeak populations for the two DGLs, and the gradient dV/dZ has values of -1.4 to -1.5 cm s^{-1} dB^{-1} in the fast-falling subpeak populations and -0.4 to -1.1 cm s^{-1} dB^{-1} in the slow-falling subpeak populations. These absolute values are smaller than those in the MPL. The small absolute values of dV/dZ are consistent with the presence of low density ice particles that can be more affected from air resistance. Considering the lack of a supercooled liquid layer in this regime, the ice particles can only grow via deposition and aggregation. In the DGL of the 24 May case, the absolute value of dV/dZ in the slow-falling subpeak populations is larger than that of the 29 April case, and the absolute value of dV/dZ in the fast-falling subpeak populations is also slightly larger. The difference in gradient suggests that heavier aggregation dominated during the 24 May case, and that light aggregation and/or depositional growth characterized slower falling subpeak populations on 29 April. The absolute value of dV/dZ of the fast-falling subpeak populations of the 29 April case is slightly smaller than that of the fast-falling subpeak populations of the 24 May case, suggesting light aggregation.

Next, the SACR2 QVP Z_{DR} and K_{DP} measurements that correspond to the observed DGLs in the two cases are examined. Figure 5 shows height-versus-time plots of QVPs of the Ka/W-SACR2 Z_{DR} and K_{DP}. Previous studies have indicated evidence of an increase in K_{DP} in a DGL around a temperature of $-15°C$ (e.g., Bechini et al., 2013; Kennedy & Rutledge, 2011; Kumjian et al., 2014), and this enhancement was associated with the appearance of multimodal Doppler spectra (e.g., Moisseev et al., 2015). Mean values of the QVPs associated with the multimodal Doppler spectra are listed in Table 1, together with KAZR fast-falling and slow-falling subpeak reflectivities and mean Doppler velocities and their dV/dZ values. A similar increase in K_{DP} is
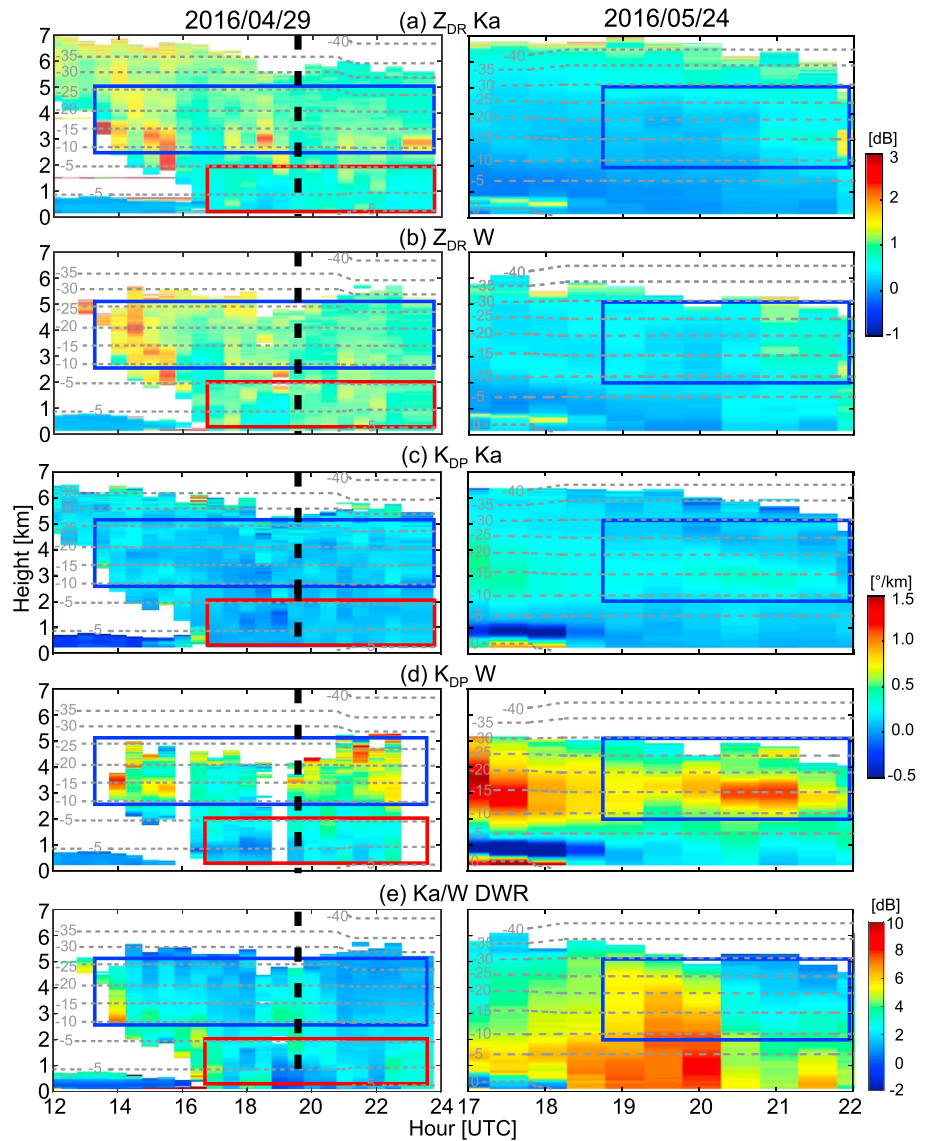
Figure 5. Height versus time cross sections of (a) Ka-SACR2 Z_{DR}, (b) W-SACR2 Z_{DR}, (c) Ka-SACR2 K_{DP}, (d) W-SACR2 K_{DP}, and (e) Ka/W-SACR2 dual-wavelength ratio (DWR) for 29 April 2016 (left column) and 24 May 2016 (right column). Gray dashed lines represent temperature with a 5 K increment from soundings at Oliktok. Blue and red boxes represent the DGLs and the MPL, respectively. Differential phase data collected by the W-SACR2 PPI at 1538, 1838, and 2238 UTC on 29 April 2016 experienced some contamination by spurious values, resulting in the data gaps in (d).

observed in both Ka- and W-SACR2 observations through the selected periods for the 29 April and 24 May cases. The K_{DP} enhancement is roughly collocated in height with multimodal spectra shown as slow-falling subpeaks in Figure 3c. For the 24 May case, the K_{DP} enhancement also coexists with Z_{DR} decreasing toward the ground while KAZR reflectivity and downward velocity increase (Figures 3a and 3b). For the 29 April case, W-SACR2 K_{DP} values in the DGL (>0.5° km^{-1}) are generally larger than those in the MPL and anticorrelated with Z_{DR}, similar to the 24 May case. For the Ka-SACR2 QVP in the 29 April DGL, the mean K_{DP} value in the DGL is slightly larger than that in the MPL (Table 1), while Z_{DR} values are slightly larger, although the enhancement of K_{DP} is very weak compared to the 24 May case.

If it is assumed that the observed K_{DP} values in the DGL were produced by highly nonspherical ice particles such as dendrites or hexagonal plates, and such particles dominated the ice in the cloud, then the expected Z_{DR} values should be much higher than the observed Z_{DR} values (i.e., greater than approximately 4 dB, e.g., Westbrook, 2014). The observed Z_{DR} and K_{DP} values suggest that at least two types of ice particles coexisted

Table 1
Mean Values of Observed Variables From KAZR Measurements and Ka/W-SACR2 QVPs, Estimated dV/dZ, and Estimated Ka-Band Intrinsic Z_{DR} Associated With Multimodal Doppler Spectra Regions for the Three Analyzed Layers

		DGL 29 April	DGL 24 May	MPL 24 April
KAZR Z_H (dBZ)	Fast falling	−4.1 (0.39)	1.1 (1.87)	−3.6 (0.48)
	Slow falling	−13.0 (0.13)	−14.2 (0.05)	−20.9 (0.03)
KAZR Doppler velocity (m s^{-1})	Fast falling	−0.87 (0.168)	−0.98 (0.174)	−0.99 (0.17)
	Slow falling	−0.43 (0.098)	−0.42 (0.144)	−0.29 (0.22)
KAZR dV/dZ (cm s^{-1} dB^{-1})	Fast falling	−1.4 (0.29)	−1.5 (0.42)	−2.0 (0.32)
	Slow falling	−0.4 (0.11)	−1.1 (0.25)	−2.5 (0.72)
QVP Z_{DR} (dB)	Ka	1.1 (0.09)	0.9 (0.08)	0.7 (0.01)
	W	1.1 (0.09)	0.9 (0.04)	0.9 (0.01)
QVP K_{DP} (° km^{-1})	Ka	0.1 (0.06)	0.2 (0.05)	0.1 (0.02)
	W	0.5 (0.12)	0.8 (0.25)	0.2 (0.03)
Estimated Ka-band intrinsic Z_{DR} (dB)	Fast falling	0.9	0.6	0.7
	Slow falling	2.1–2.6	2.8–3.8	

Note. Numbers in parentheses for the Ka-band ARM Zenith pointing Radar (KAZR) Z_H and Doppler velocity represent standard deviations in the analyzed layers; those for KAZR dV/dZ represent coefficients of determination, and those for quasi-vertical profile (QVP) Z_{DR} and QVP K_{DP} represent mean values of standard deviation over azimuth angle from QVP estimates. The standard deviations of SACR2 Z_{DR} and KAZR Z_H are in linear scale. DGL = dendritic/planar crystal growth layer.

in the multimodal spectra regions and that these had different contributions to Z_{DR} and K_{DP}. Large and more isotropic particles, such as irregular or aggregated ice usually produce low Z_{DR} because of their low density and relatively high aspect ratio. The aspect ratios of aggregates generally vary between 0.5 and 0.7 (Hogan et al., 2012; Korolev & Isaac, 2003) and can be smaller than 0.6 (Jiang et al., 2017). These quasi-isotropic ice particles, having aspect ratios less than 1, can produce tangible K_{DP} if their concentration is sufficiently high. Once such particles (with aspect ratios <1) fall through the DGL, they experience vigorous depositional growth in a high supersaturation environment. Sounding measurements at 1800 UTC on those days shows that the DGLs included regions of sufficient supersaturation with respect to ice (Figure 2). Generally, the value of K_{DP} of quasi-isotropic particles increases as their ice water content (IWC) increases, as shown by increase in total reflectivity from KAZR measurements in the DGL. Their aggregation is facilitated near the bottom of the DGL through collisions with similar particles and newly generated and slowly falling dendrites having branches facilitating interlocking (Pruppacher & Klett, 2010). The aggregation process leads to the reduction in ice/snow density, resulting in decreased Z_{DR}.

Additional increase of K_{DP} can be attributed to plate-like crystals like hexagonal plates or dendrites with very nonspherical shapes which start growing locally at the DGL. The Doppler velocity associated with slow-falling subpeaks is consistent with the typical particle fall velocity of dendrite/plate crystals (Kajikawa, 1989). Dendrite/plate crystals (plate-like crystals in this study) have very high intrinsic Z_{DR}, but the total Z_{DR} in the radar volume can be quite low if these crystals are mixed with quasi-spherical ice particles in much higher concentration. In the DGLs in our analysis, the reflectivities from the slow-falling subpeaks are much lower than those from the faster-falling subpeaks (e.g., Figure 1a and Table 1), and the observed Z_{DR} is lower than the intrinsic Z_{DR} of plate-like crystals (e.g., Westbrook, 2014). Therefore, the smaller plate-like crystals likely coexisted with larger quasi-spherical ice particles.

Comparing the 29 April with 24 May cases, the observed Z_{DR} values for the 29 April case are larger, whereas the K_{DP} values are smaller. These larger Z_{DR} and smaller K_{DP} values on 29 April suggest lower number concentration of quasi-isotropic ice particles, which results in a decreased K_{DP} and increased Z_{DR} due to a larger relative contribution of plate-like crystals. On the other hand, the Z_{DR} and K_{DP} values for the 24 May case are indicative of higher number concentration of quasi-isotropic particles producing larger K_{DP}, and smaller Z_{DR}. The MASC observed larger aggregates at the surface on 24 May, consistent with the radar polarimetric and spectral signatures.

The DWR also points to this difference in the intensity of aggregation. The DWR in DGL (Figure 5e) generally correlates with reflectivity (Figure 3a), and the DWR values in the 24 May case is larger than those in the 29 April case. DWR is color coded in the KAZR reflectivity-KAZR Doppler velocity plane for the DGLs of the two cases in Figure 6. In the 24 May case (Figure 6b), much larger values of DWR (exceeding 5 dB) associated with higher reflectivity (>2 dBZ) are measured than in the 29 April case, suggesting large aggregates. The large
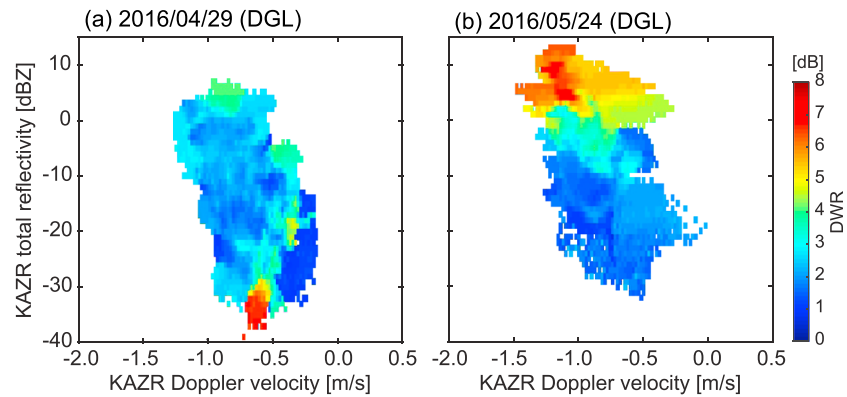
Figure 6. Ka-band ARM Zenith pointing Radar (KAZR) total reflectivity versus KAZR mean Doppler velocity plots for (a) the 29 April case and (b) the 24 May case. Color shade represents corresponding mean dual-wavelength ratio (DWR) from SACR2 quasi-vertical profiles. DGL = dendritic/planar crystal growth layer.

DWR tends to have higher fall speeds (downward Doppler velocities) which are greater than 0.7 m s^{-1}. In the 29 April case (Figure 6a), DWR is less than 4 dB with KAZR reflectivity >-15 dBZ even for fall speeds (downward Doppler velocities) greater than 0.7 m s^{-1}. This suggests that compact, smaller ice particles dominated in the 29 April case in full accordance with MASC images displayed in Figure 3d. Considering the lack of supercooled liquid droplets in the layers, the observed DWR in the 24 May case is likely produced by large aggregates (e.g., Kneifel et al., 2015; Leinonen & Szyrmer, 2015; Tyynelä et al., 2011) rather than spherical rimed particles (e.g., Kneifel et al., 2015; Kneifel et al., 2016). Some larger DWR values with lower reflectivity (<-15 dBZ) are found in the plot for the 24 April case (especially around KAZR reflectivity of -35 dBZ and KAZR Doppler velocity of -0.7 m s^{-1}). These values originate from the Ka/W-SACR2 QVPs at 1316 and 1346 UTC, where larger Ka/W-SACR2 QVP Z_{DR} values (>1.7 dB, Ka-SACR2 Z_{DR} attained >4 dB at 1316 UTC) accompanying the low reflectivity values were observed. These larger Ka-band Z_{DR} collocated with low reflectivity suggests very low number concentration of plate-like crystals, which produced large DWR due to non-Rayleigh scattering effects (e.g., Lu et al., 2013). Lu et al. (2013) showed that the non-Rayleigh scattering effects of plate-like crystals at W band are significant when the maximum dimension of crystals is greater than 2 mm. In the 24 May case, the DWR values above the melting layer (1700–1845 UTC) are relatively small (Figure 5e) likely due to effects of rain attenuation and non-Rayleigh scattering.

In Figures 5c and 5d, a couplet of large positive and negative K_{DP} is observed within the lowest 1 km layer near the surface on 24 May during the time interval from 1700 to 1800 UTC. This is an artifact of the K_{DP} processing routine which portrays the melting layer with significant value of the backscatter differential phase. A more sophisticated routine for the processing of differential phase allows the elimination of such artifacts (Griffin et al., 2017).

To quantify the extent to which smaller particles contribute to Z_{DR} in the multimodal Doppler spectra cases, the Ka-SACR2 Z_{DR} versus ratio of radar reflectivities associated with the fast-falling subpeaks and slow-falling subpeaks is shown in Figures 7a and 7b. In the DGLs, Z_{DR} tended to increase when reflectivities from slow-falling subpeaks approached those from fast-falling subpeaks. This result supports the notion that slow-falling particles have more oblate shapes than fast-falling, quasi-isotropic ones and that the slow-falling oblate particles could contribute more to the observed Z_{DR} when their reflectivity relative to the faster-falling particles is increased.

3.2. Mixed-Phase Layer

One of the distinct differences between the MPL and DGL is a larger gradient in the velocity-reflectivity relationship (approximately 2 cm s^{-1} dB^{-1}, Figures 4e and 4f) in the MPL for both slow- and fast-falling Doppler spectra subpeaks. The larger gradient indicates that the particles have a faster fall velocity at a given reflectivity, suggesting compact, high-density particles. The probability density distributions of KAZR reflectivity versus KAZR mean Doppler velocity from the secondary peak are combined in Figures 4e and 4f. The Doppler spectra in this layer reveal a cloud droplet signature in slow-falling subpeaks and secondary peaks,
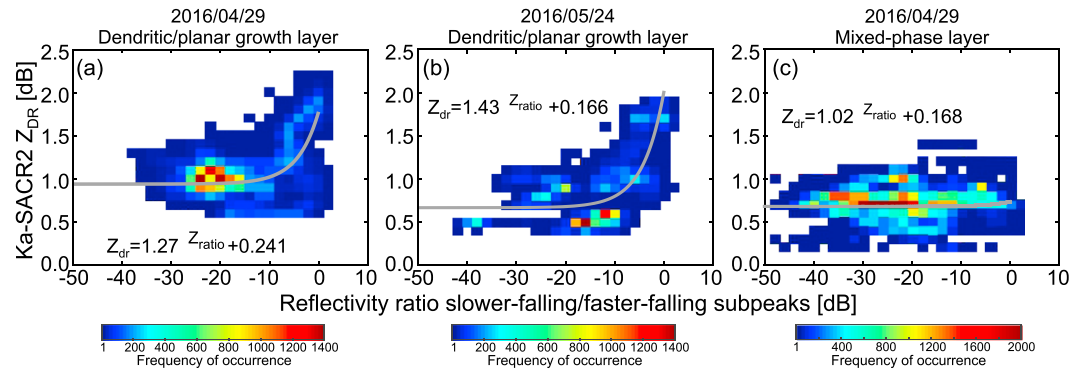
Figure 7. Ka-SACR2 Z_{DR} versus reflectivity ratio of slow-falling subpeak to fast-falling subpeak (Z_{ratio}) plots for (a) the dendritic/planar crystal growth layer of 29 April 2016 (blue box in Figure 3c, left column and in Figure 5a, left column), (b) the dendritic/planar crystal growth layer of 24 May 2016 (blue box in Figure 3c, right column and Figure 5a, right column), and (c) the mixed-phase layer of 29 April 2016 (red box in Figure 3c, left column and Figure 5a, left column). The best fit line (gray) and its equation are also shown in each panel. Z_{dr} and Z_{ratio} in the equations are in linear scale. Color shades represent the number of samples.

which have near 0.0 m s^{-1} mean Doppler velocity (mostly ranging from -0.3 to 0.2 m s^{-1}) and low reflectivity (less than -25 dBZ). The variability of the apparent Doppler velocity associated with cloud droplets suggests vertical air motions (e.g., Shupe et al., 2004). The ice particles could effectively grow by riming in the MPL.

Compared with the DGL, K_{DP} values in the MPL are lower ($<0.1°$ km^{-1} at Ka band; $<0.3°$ km^{-1} at W band); most of the values are close to 0.0° km^{-1} in Figures 5c and 5d. This difference is clearly obvious at W band. The MPL also showed slightly lower Z_{DR} (Figure 5a). These K_{DP} and Z_{DR} values suggest that the primary peaks were composed of isotropic particles in fast- and slow-falling subpeaks. The Ka-SACR Z_{DR} versus reflectivity ratio of slow-falling subpeaks to fast-falling subpeaks in the MPL generally shows low Z_{DR} regardless of reflectivity ratio (Figure 7c). This plot indicates that compact, more isotropic particles with low Z_{DR} are dominant in both fast-falling and slow-falling subpeaks in the MPL. Any interdependencies of Z_{DR} and K_{DP} are less pronounced in the MPL than in the DGL primarily due to lower magnitudes of Z_{DR} and K_{DP}.

One more noteworthy signature in the MPL is a slight increase in Z_{DR} that is somewhat visible in Figure 5a and is clearly shown in Figure 1b at 2 km with temperatures around $-5°$C. Increased values of Z_{DR} (roughly 1.0–1.2 dB) clearly shown in the MPL tops (Figure 1b) are consistent with needle and/or columnar crystals with nearly random orientation in the horizontal plane (Matrosov, 1991). The signature of needle and/or columnar crystals in a temperature range from -8 to $-3°$C, where ice particles seeded in the MPL and secondary ice formation via the Hallett-Mossop ice multiplication mechanism (Hallett & Mossop, 1974) could be active, is often observed in Arctic mixed-phase clouds in linear depolarization ratio measurements (Oue, Kumjian, Lu, Verlinde, et al., 2015). Similar signatures were observed in midlatitude winter storms and convective systems (e.g., Giangrande, Toto, Bansemer, et al., 2016; Kumjian et al., 2016; Kumjian & Lombardo, 2017; Sinclair et al., 2016; Zawadzki et al., 2001). Kumjian et al. (2016) observed K_{DP} enhancements produced by needle and columnar crystals in secondary ice formation regions. In the present study, similar slightly enhanced K_{DP} values at Ka band are found at altitudes below 1 km in the 29 April case (Figure 1b). This enhancement is caused by possible presence of secondary ice with very elongated shapes (e.g., needles or columns).

4. Discussion

The results of the first combined polarimetric and Doppler spectral radar measurements in precipitating deep Arctic clouds presented herein are generally in agreement with previous studies performed in midlatitude stratiform clouds using longer-wavelength radars operating at S, C, and X bands (e.g., Andrić et al., 2013; Bechini et al., 2013; Griffin et al., 2017; Kennedy & Rutledge, 2011; Moisseev et al., 2015; Schrom et al., 2015; Schrom & Kumjian, 2016; Thompson et al., 2014; Williams et al., 2015). All of these studies document notable enhancement of Z_{DR} and/or K_{DP} in the DGL although the Z_{DR} and K_{DP} signatures may not occur simultaneously and not be collocated. In the present study, notable enhancement of K_{DP} combined with relatively
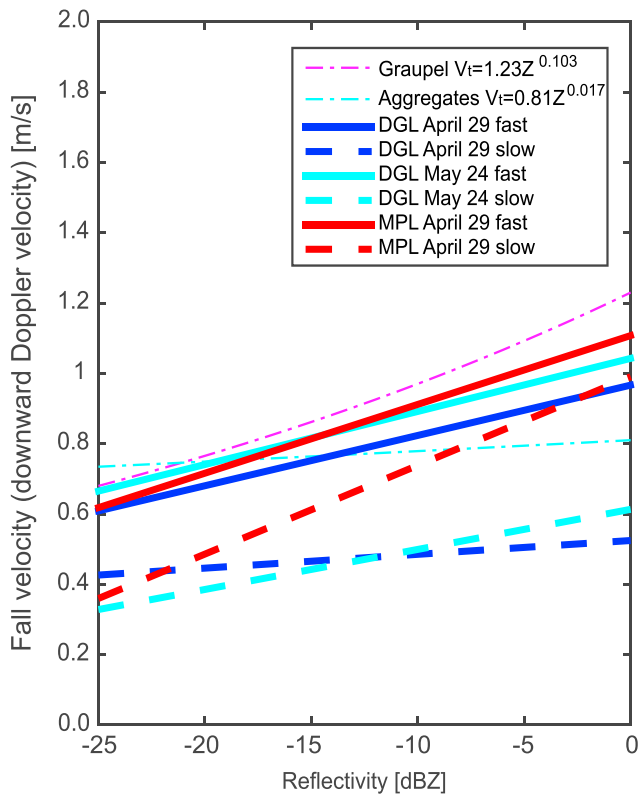
Figure 8. Comparison of Doppler velocity-reflectivity relationships in this study with terminal fall velocity (V_t)-reflectivity (Z) relationships for graupel and aggregates presented by Straka et al. (2000). The unit of Z of the graupel and aggregate V_t-Z relationships in the legend is $mm^{-6} m^{-3}$. Downward Doppler velocity is represented by positive values in this plot. DGL = dendritic/planar crystal growth layer; MPL = mixed-phase layer.

low Z_{DR} is found in the Ka/W-SACR2 QVPs for the 24 May DGL, while the enhancement of K_{DP} is small but Z_{DR} is relatively high in the 29 April DGL. These signatures were originally attributed to the existence of plate-like pristine crystals such as dendrites and hexagonal plates that predominantly grow in the DGL. A quite different interpretation has recently been proposed by Moisseev et al. (2015) who claim that increased K_{DP} is "an indicator of the onset of aggregation rather than an indicator of a dendritic growth zone". This view is shared by Griffin et al. (2017), who emphasized strong anticorrelation between Z_{DR} and K_{DP} in the dendritic growth layer and also found a clear link between the height of the top of the cloud and the magnitudes of K_{DP} and Z_{DR} within the dendritic growth layer. According to Griffin et al. (2017), colder cloud tops favor higher K_{DP} resulting from high number concentration of seeding ice particles, whereas the highest values of Z_{DR} were observed in clouds with little ice above DGL.

A link between the K_{DP} and Z_{DR} signatures in the DGL and the temperature at the top of the cloud is also revealed in the Arctic deep clouds examined in this study. For most of the duration of the 24 May event, the cloud top was colder than for the 29 April event. Although the temperature difference was not large (5 K on average), it is important that the cloud top on 24 May was persistently colder than −35 to −38°C— a temperature interval where homogeneous ice nucleation takes place. Primary ice in very high concentration produced by homogeneous nucleation (e.g., DeMott et al., 2010; Jeffery & Austin, 1997) fell through the DGL and resulted in higher ice water content and higher reflectivity factor observed in the 24 May case compared to the 29 April event. Primary ice in the DGL commonly has relatively high aspect ratio (0.5–0.7 according to Korolev & Isaac, 2003) and does not produce very high values of Z_{DR}. However, its K_{DP} can be significant, due to high concentration of ice, and such enhancement is particularly visible near the lower part of the DGL where primary ice particles become larger. If the amount of ice seeding the DGL from above is not large, then this type of ice may not mask locally grown ice (dendrites and hexagonal plates) which has high inherent Z_{DR} due to much lower aspect ratios but much lower K_{DP} since its concentration is usually low. This is what was observed during the 29 April event. More discussion on the nature of these microphysical processes and related polarimetric signatures can be found in Griffin et al. (2017).

Many studies have examined terminal fall velocity as a function of radar reflectivity to identify ice particle types (e.g., Protat & Williams, 2011; Straka et al., 2000). Figure 8 shows terminal fall velocity (V_t)-reflectivity (Z) relationships for aggregates and graupel presented by Straka et al. (2000), together with Doppler velocity (V)-reflectivity (Z) relationships from the present study. In the plots, downward Doppler velocity is represented by positive values. The graupel's V_t-Z relationship is very close to the V-Z relationship for the fast-falling subpeak populations in the MPL, and its slope is similar to the V-Z relationship for the slow-falling subpeak populations in the MPL. The slope of the aggregate's V_t-Z relationship is close to that of the V-Z relationships for the slow-falling subpeak populations in the DGLs for both the 29 April and 24 May cases, although the V_t values are larger than downward Doppler velocities from the DGL slow-falling subpeaks. The Doppler velocities of the slow-falling subpeak can be lower than the terminal velocity V_t for aggregates due to the influence of vertical air motion. The downward Doppler velocities from the DGL slow-falling subpeaks are consistent with a V_t range typical for ice particles growing by vapor deposition and having reflectivity of −10 to 0 dBZ (0.35–0.8 m s^{-1}, Protat & Williams, 2011).

Larger gradients of Doppler velocity versus reflectivity for riming cases in the MPL than those for vapor deposition and aggregation cases in the DGL were also observed in midlatitude winter storms and mesoscale convection cases (e.g., Giangrande, Toto, Jensen, et al., 2016; Schrom & Kumjian, 2016; Zawadzki et al., 2001).

Schrom and Kumjian (2016) calculated vertical gradients of reflectivity, Doppler velocity, and Z_{DR} for dendrite and isometric (assuming aggregate and/or graupel) particles and showed that they can be used to distinguish the vapor depositional growth from riming and/or aggregation processes. They suggested that these gradients are dependent on initial reflectivity values (i.e., seeding of ice from the top of the cloud), as confirmed by larger dV/dZ gradient for the 24 May DGL than for the 29 April DGL in the present study.

A major difference between the examined precipitating deep Arctic cloud systems and midlatitude snow-storm cases is that the observed reflectivity is much weaker (generally <15 dBZ) than in the midlatitude cases (>20 dBZ). The weaker reflectivity and lower IWC, which are common in Arctic clouds, result in lower sensitivity of the K_{DP} measurements if performed by longer-wavelength radars operating at X, C, or S band (Oue et al., 2016). K_{DP} values are proportional to the radar frequency in the case of Rayleigh scattering. For instance, a K_{DP} value measured by Ka-SACR2 at 1730 UTC on 24 May is approximately 0.5° km^{-1} consistent with 1.3° km^{-1} from W-SACR2. These Ka- and W-band K_{DP} values correspond to equivalent K_{DP} of 0.04° km^{-1} at S band and 0.13° km^{-1} at X band, suggesting that very careful processing of differential phase is needed for Arctic cloud observations by longer-wavelength radars. The weak reflectivity clouds also produce smaller ice particles with lower terminal velocities (1–1.5 m s^{-1}) in the riming and aggregation cases compared to the midlatitude cases (>2 m s^{-1}, e.g., Giangrande, Toto, Jensen, et al., 2016; Schrom & Kumjian, 2016) and smaller dV/dZ values likely due to weaker seeding from aloft (Schrom & Kumjian, 2016).

A big advantage of the joint analysis of Doppler spectra and polarimetric QVPs is an ability to separate the contributions to Z_H from the fast- and slow-falling ice particles as demonstrated in Figure 7. To separately compute polarimetric variables from different particle populations, many assumptions are needed (e.g., particle size distributions, fractions of the different ice particle populations in number concentrations, and reflectivity), as presented in Schrom et al. (2015) and Oue et al. (2016). The ratio of radar reflectivities from the two habits (Z_{ratio}) and the relationships between Z_{ratio} and observed Z_{DR} illustrated in Figure 7 provide necessary constraints to separately estimate Z_{DR} values attributed to the slow-falling particle populations in the DGL, following the logic of Schrom et al. (2015) and Oue et al. (2016). Assuming that the total reflectivity is a sum of the contributions from the two types of ice particle populations (i.e., fast- and slow-falling particles), the observed Z_{DR} ($Z_{dr}{}^o$ in linear scale) can be expressed in linear scale as:

$$Z_{dr}{}^o = \frac{Z_h{}^F + Z_h{}^S}{Z_v{}^F + Z_v{}^S} \tag{1}$$

where Z_h and Z_v are the reflectivities at horizontal and vertical polarizations, respectively, expressed in linear scale. Their superscripts represent fast-falling (F) or slow-falling (S) particle populations. Since the ratio of radar reflectivities associated with the fast-falling subpeaks and slow-falling subpeaks (Z_{ratio}) and differential reflectivity from the fast-falling particle population ($Z_{dr}{}^F$) are respectively

$$Z_{ratio} = \frac{Z_h{}^S}{Z_h{}^F} \tag{2}$$

and

$$Z_{dr}{}^F = \frac{Z_h{}^F}{Z_v{}^F}, \tag{3}$$

the differential reflectivity from the slow-falling particle population ($Z_{dr}{}^S$) is expressed as

$$Z_{dr}{}^S = \frac{Z_{dr}{}^o Z_{dr}{}^F Z_{ratio}}{Z_{dr}{}^F (1 + Z_{ratio}) - Z_{dr}{}^o}. \tag{4}$$

Assuming that the contribution from slow-falling particle populations to the total reflectivity can be ignored if Z_{ratio} is small enough (e.g., <−20 dB), $Z_{dr}{}^F$ values in the DGLs for the two cases are approximately 1.2 (0.9 dB) for the 29 April case (Figure 7a) and 1.1 (0.6 dB) for the 24 May case (Figure 7b). Figure 9 shows $Z_{dr}{}^o$ ($Z_{DR}{}^o$ in dB scale) versus Z_{ratio} diagrams for these two $Z_{dr}{}^F$ values, where shades represent $Z_{dr}{}^S$ values ($Z_{DR}{}^s$ in dB scale). Black lines on these plots represent $Z_{dr}{}^o$-Z_{ratio} relations estimated from Figures 7a and 7b:

$$Z_{dr}{}^o = 1.27^{Z_{ratio}} + 0.241 \text{ for the 29 April case, and}$$

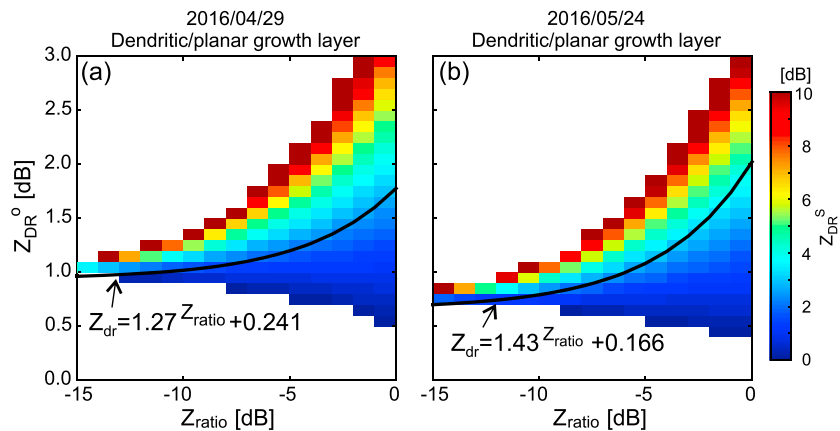$$Z_{dr}{}^o = 1.43^{Z_{ratio}} + 0.166 \text{ for the 24 May case.}$$

Figure 9. Z_{DR} values for slower-falling particle populations (Z_{DR}^S, shade) in dendritic/planar crystal growth layers calculated from Z_{ratio} and total Z_{DR} (Z_{DR}^o) for (a) the 29 April and (b) the 24 May case. Here Z_{DR} values for faster-falling particle populations (Z_{DR}^F) were assumed to be 0.9 dB for the 29 April and 0.6 dB for the 24 May case. Black curves represent Z_{DR}^F-Z_{ratio} relationships presented in Figures 7a and 7b, respectively.

According to these relations, Z_{DR}^S values with $Z_{ratio} > -5$ dB are 2.1–2.6 dB for the 29 April case and 2.8–3.3 dB for the 24 May case. These Z_{DR} values suggest small plate-like crystals and/or light aggregation of these crystals (e.g., Oue et al., 2016). The estimated Z_{DR}^S values for the 24 May case are slightly larger than those for the 29 April case, suggesting that dense, larger dendrites were produced, facilitating aggregation.

The QVP technique assumes that the horizontal variability of polarimetric radar variables within the area of azimuthal averaging is relatively small. In order to control horizontal inhomogeneity, the standard deviations of the Z_{DR} and K_{DP} estimates resulting from azimuthal variability have been computed and presented in Table 1. The standard deviations over azimuth angle were found to be generally 10 times smaller than the mean values of Z_{DR} QVP and 2–4 times smaller than the mean values of K_{DP} QVP in both events analyzed in this study. The relatively small standard deviations of the Z_{DR} and K_{DP} estimates attest to the fact that the QVP polarimetric signatures are meaningful, but certain caution has to be exercised in their interpretation.

5. Summary

The study of Arctic ice and mixed-phase clouds using millimeter-wavelength radars is an area of active and challenging research. The challenge arises from several factors including low reflectivity, large natural variability of the observed ice particle properties (mass, density, and shape), the variability of ice particle size distributions, the complexity of ice and mixed-phase microphysical processes, and uncertainties in the estimation of particle scattering properties. Dual-polarization and multifrequency Doppler radar observations hold great promise to improve our qualitative and quantitative understanding of ice and mixed-phase processes. The profiling and scanning millimeter-wavelength radars at the ARM Oliktok site provide such observations well matched in time and space. The combination of radar Doppler spectra with radar polarimetric observations improves the identification of ice particles and their characteristics such as shape and fall speed in mixed ice particle regions, through the synergistic use of KAZR Doppler spectra and Ka/W-SACR2 QVP of polarimetric radar variables at the same height. The results presented in this study illustrate the frequent occurrence of multimodal radar Doppler spectra in the DGL in these Arctic deep cold precipitating systems. The multimodality of the Doppler spectra is caused by particle populations well separated in their fall velocity: quasi-spherical aggregated or irregular ice seeded from above and locally generated, slow-falling, plate-like particles with very low aspect ratio. It is shown that for a cloud with a colder top, fast-falling quasi-isotropic ice particles (with aspect ratio < 1) dominate and the corresponding K_{DP} is high due to the high concentration of the particles whereas Z_{DR} is low. For a cloud with warmer cloud top temperatures, the opposite is true: K_{DP} is low and Z_{DR} is high due to a larger contribution from anisotropic slow-falling ice and lower overall concentration of ice particles. Such a pattern is commonly observed in the midlatitude precipitating stratiform clouds in the cold season as well (Griffin et al., 2017).

Another area favoring the occurrence of multimodal Doppler spectra is the MPL, where particle fall speeds were higher than those in the DGL and the enhancements of K_{DP} and Z_{DR} were weak, suggesting that compact, high-density, spherical particles dominated and those with different sizes were mixed together. Slight increases of K_{DP} and Z_{DR} in the MPL suggest a possible growth of columnar and/or needle crystals via secondary ice nucleation or local generation of elongated prolate ice within the temperature interval centered at −5°C.

A key point illustrated in this study is that the joint analysis of the Doppler spectra peak properties and polarimetric radar variables can improve the interpretation of the radar measurements in the DGL and MPL, and the quantification of the contributions of different ice habits to the total values of radar reflectivity, differential reflectivity, and specific differential phase. This will lead to better polarimetric estimation of the ice water content compared to the earlier studies of Vivekanandan et al. (1994) and Ryzhkov et al. (1998). To understand formation and growth processes of these ice particles, wind shear and time evolution should be considered (e.g., Kalesse et al., 2016; Pfitzenmaier et al., 2017) and the QVP data should be updated over shorter time intervals. The presented study introduces a new approach in analyzing ice and mixed-phase microphysics using the combination of radar Doppler spectra and polarimetric observations. Polarimetric Doppler spectra measurements are expected to improve the estimations of polarimetric variables and IWC for different ice types in the mixed ice volume (e.g., Moisseev & Chandrasekar, 2007; Unal, 2015).

The subject of developing realistic, well-validated, scattering libraries at high radar frequencies has gained popularity during last few years, mainly due to the availability of high quality, multiwavelength polarimetric and Doppler radar observations coupled with in situ, ground-based observations of ice particle properties (Kneifel et al., 2015, 2016; Moisseev et al., 2015). In addition, we make coordinated efforts to consolidate all of the available scattering libraries (e.g., Kneifel et al., 2017; Leinonen & Moisseev, 2015; Leinonen & Szyrmer, 2015; Lu et al., 2016). The scattering calculations and their libraries can be used to complement the discussion based on the results of observations and provide some clues on better understanding and interpretation of the radar data (see Text S1 and Figures S1 and S2 in the supporting information). In this study, we focus on Doppler velocity information and its use to infer the ice particle properties in combination with polarimetric data. Information about particle shape, fall speeds, and fraction of mixed ice particles from the observation can allow reducing uncertainties in the scattering calculation analysis. Naturally, the use of multimodal radar Doppler spectra is complementary to the multiwavelength polarimetric radar approach to the identification of ice particles properties; hence, well-validated scattering libraries are needed for any quantitative retrievals. Our future work will aim at combining these two approaches. Finally, the study is far from being comprehensive; rather, it introduces only some of the many possible applications for which radar Doppler spectra and polarimetric measurements can be utilized.

References

Andrić, J., Kumjian, M. R., Zrnić, D., Straka, J. M., & Melnikov, V. (2013). Polarimetric signatures above the melting layer in winter storms: An observational and modeling study. *Journal of Applied Meteorology and Climatology*, *52*(3), 682–700. https://doi.org/10.1175/JAMC-D-12-028.1

ARM Climate Research Facility (2013a). Updated hourly. Ceilometer (CEIL). 2016-04-29 and 2016-05-24, ARM Mobile Facility (OLI) Oliktok Point, Alaska; AMF3 (M1). Compiled by B. Ermold and V. Morris. Atmospheric Radiation Measurement (ARM) Climate Research Facility Data Archive. Oak Ridge, TN. Data available at 2017–04-24 Retrieved from https://doi.org/10.5439/1181954

ARM Climate Research Facility (2013b). Updated hourly. Microwave Radiometer, 3 Channel (MWR3C). 2016-04-29 and 2016-05-24, ARM Mobile Facility (OLI) Oliktok Point, Alaska; AMF3 (M1). Compiled by M. Cadeddu. Atmospheric Radiation Measurement (ARM) Climate Research Facility Data Archive. Oak Ridge, TN. Retrieved from https://doi.org/10.5439/1025248

ARM Climate Research Facility. (2013c). Updated hourly. Balloon-Borne Sounding System (SONDEWNPN). 2016-04-29 and 2016-05-24, ARM Mobile Facility (OLI) Oliktok Point, Alaska; AMF3 (M1). Compiled by D. Holdridge, J. Kyrouac and R. Coulter. Atmospheric Radiation Measurement (ARM) Climate Research Facility Data Archive. Oak Ridge, TN. Retrieved from https://doi.org/10.5439/1021460

ARM Climate Research Facility (2016a). Updated hourly. Ka-Band Scanning ARM Cloud Radar (KASACRPPIVH). 2016-04-29 and 2016-05-24, ARM Mobile Facility (OLI) Oliktok Point, Alaska; AMF3 (M1). Compiled by A. Matthews, B. Isom, D. Nelson, I. Lindenmaier, J. Hardin, K. Johnson and N. Bharadwaj. Atmospheric Radiation Measurement (ARM) Climate Research Facility Data Archive. Oak Ridge, TN.

ARM Climate Research Facility (2016b). Updated hourly. W-band Scanning ARM Cloud Radar (WSACRPPIVH). 2016-04-29 and 2016-05-24, ARM Mobile Facility (OLI) Oliktok Point, Alaska; AMF3 (M1). Compiled by A. Matthews, B. Isom, D. Nelson, I. Lindenmaier, J. Hardin, K. Johnson and N. Bharadwaj. Atmospheric Radiation Measurement (ARM) Climate Research Facility Data Archive. Oak Ridge, TN.

Aydin, K., Verlinde, J., Clothiaux, E. E., Lu, Y., Jiang, Z., & Botta, G. (2016). Polarimetric scattering database for non-spherical ice particles at microwave wavelengths. Atmospheric Radiation Measurement (ARM) Climate Research Facility Data Archive. Oak Ridge, TN. Retrieved from https://doi.org/10.5439/1258029

Bechini, R., Baldini, L., & Chandrasekar, V. (2013). Polarimetric radar observations in the ice region of precipitating clouds at C-band and X-band radar frequencies. *Journal of Applied Meteorology and Climatology*, *52*(5), 1147–1169. https://doi.org/10.1175/JAMC-D-12-055.1

Cesana, G., Kay, J. E., Chepfer, H., English, J. M., & de Boer, G. (2012). Ubiquitous low-level liquid-containing Arctic clouds: New observations and climate model constraints from *CALIPSO*-GOCCP. *Geophysical Research Letters*, *39*, L20804. https://doi.org/10.1029/2012GL053385

DeMott, P., Prenni, A., Liu, X., Kredenweis, S., Pettres, M., Twohy, C., et al. (2010). Predicting global atmospheric ice nuclei distributions and their impacts of climate. *Proceedings of the National Academy of Sciences of the United States of America*, *107*(25), 11,217–11,222. https://doi.org/10.1073/pnas.0910818107

Garrett, T. J., Yuter, S. E., Fallgatter, C., Shkurko, K., Rhodes, S. R., & Endries, J. L. (2015). Orientations and aspect ratios of falling snow. *Geophysical Research Letters*, *42*, 4617–4622. https://doi.org/10.1002/2015GL064040

Giangrande, S., Toto, T., Bansemer, A., Kumjian, M., Mishra, S., & Ryzhkov, A. (2016). Insights Into riming and aggregation processes as revealed by aircraft, radar, and disdrometer observations for a 27 April 2011 widespread precipitation event. *Journal of Geophysical Research: Atmospheres*, *121*, 5846–5863. https://doi.org/10.1002/2015JD024537

Giangrande, S. E., Toto, T., Jensen, M. P., Bartholomew, M. J., Feng, Z., Protat, A., et al. (2016). Convective cloud vertical velocity and mass-flux characteristics from radar wind profiler observations during GoAmazon2014/5. *Journal of Geophysical Research: Atmospheres*, *121*, 12,891–12,913. https://doi.org/10.1002/2016JD025303

Griffin, E., Schuur, T., & Ryzhkov, A. (2017). A polarimetric analysis of ice microphysical processes in snow, using quasi-vertical profiles. *Journal of Applied Meteorology and Climatology*, *57*(1), 31–50. https://doi.org/10.1175/JAMC-D-17-0033.1

Hall, M. P. M., Goddard, J. W. F., & Cherry, S. M. (1984). Identification of hydrometeors and other targets by dual-polarization radar. *Radio Science*, *19*(1), 132–140. https://doi.org/10.1029/RS019i001p00132

Hallett, J., & Mossop, S. C. (1974). Production of secondary ice particles during the riming process. *Nature*, *249*(5452), 26–28. https://doi.org/10.1038/249026a0

Hogan, R., Tian, L., Brown, P., Westbrook, C., Heymsfield, A., & Eastment, J. (2012). Radar scattering from ice aggregates using the horizontally aligned oblate spheroid approximation. *Journal of Applied Meteorology and Climatology*, *51*(3), 655–671. https://doi.org/10.1175/JAMC-D-11-074.1

Hubbert, J. C., & Bringi, V. N. (1995). An iterative filtering technique for the analysis of copolar differential phase and dual-frequency radar measurements. *Journal of Atmospheric and Oceanic Technology*, *12*(3), 643–648. https://doi.org/10.1175/1520-0426(1995)012%3C0643:AIFTFT%3E2.0.CO;2

Jayaweera, K., & Ohtake, T. (1973). Concentration of ice crystals in Arctic stratus clouds. *Journal of Research Atmosphere*, *7*, 199–207.

Jeffery, C. A., & Austin, P. H. (1997). Homogeneous nucleation of supercooled water: Results from a new equation of state. *Journal of Geophysical Research*, *102*(D21), 25,269–25,279. https://doi.org/10.1029/97JD02243

Jiang, Z., Oue, M., Verlinde, J., Clothiaux, E. E., Aydin, K., Botta, G., & Lu, Y. (2017). What can we conclude about the real aspect ratios of ice particle aggregates from two-dimensional images? *Journal of Applied Meteorology and Climatology*, *56*(3), 725–734. https://doi.org/10.1175/JAMC-D-16-0248.1

Kajikawa, M. (1989). Observation of the falling motion of early snowflakes. Part II: On the variation of falling velocity. *Journal of the Meteorological Society of Japan*, *67*(5), 731–738. https://doi.org/10.2151/jmsj1965.67.5_731

Kalesse, H., Kollias, P., & Szyrmer, W. (2013). On using the relationship between Doppler velocity and radar reflectivity to identify microphysical processes in midlatitudinal ice clouds. *Journal of Geophysical Research: Atmospheres*, *118*, 12,168–12,179. https://doi.org/10.1002/2013JD020386

Kalesse, H., Szyrmer, W., Kneifel, S., Kollias, P., & Luke, E. (2016). Fingerprints of a riming event on cloud radar Doppler spectra: observations and modeling. *Atmospheric Chemistry and Physics*, *16*(5), 2997–3012. https://doi.org/10.5194/acp-16-2997-2016

Karlsson, J., & Svensson, G. (2011). The simulation of Arctic clouds and their influence on the winter surface temperature in present-day climate in the CMIP3 multi-model dataset. *Climate Dynamics*, *36*(3-4), 623–635. https://doi.org/10.1007/s00382-010-0758-6

Kennedy, P. C., & Rutledge, S. A. (2011). S-band dual-polarization radar observations of winter storms. *Journal of Applied Meteorology and Climatology*, *50*(4), 844–858. https://doi.org/10.1175/2010JAMC2558.1

Khain, A. P., Beheng, K. D., Heymsfield, A., Korolev, A., Krichak, S. O., Levin, Z., et al. (2015). Representation of microphysical processes in cloud-resolving models: Spectral (bin) microphysics versus bulk parameterization. *Reviews of Geophysics*, *53*, 247–322. https://doi.org/10.1002/2014RG000468

Kneifel, S., Dias Neto, J., Ori, D., Moisseev, D., Tyynelä, J., Adams, I., et al. (2017). The first international summer snowfall workshop: Scattering properties of realistic frozen hydrometeors from simulations and observations, as well as defining a new standard for scattering databases. *Bulletin of the American Meteorological Society*. https://doi.org/10.1175/BAMS-D-17-0208.1

Kneifel, S., Kollias, P., Battaglia, A., Leinonen, J., Maahn, M., Kalesse, H., & Tridon, F. (2016). First observations of triple-frequency radar Doppler spectra in snowfall: Interpretation and applications. *Geophysical Research Letters*, *43*, 2225–2233. https://doi.org/10.1002/2015GL067618

Kneifel, S., Lerber, A., Tiira, J., Moisseev, D., Kollias, P., & Leinonen, J. (2015). Observed relations between snowfall microphysics and triple-frequency radar measurements. *Journal of Geophysical Research: Atmospheres*, *120*, 6034–6055. https://doi.org/10.1002/2015JD023156

Kollias, P., Bharadwaj, N., Widener, K., Jo, I., & Johnson, K. (2014). Scanning ARM cloud radars. Part I: Operational sampling strategies. *Journal of Atmospheric and Oceanic Technology*, *31*(3), 569–582. https://doi.org/10.1175/JTECH-D-13-00044.1

Kollias, P., Clothiaux, E. E., Miller, M. A., Luke, E. P., Johnson, K. L., Moran, K. P., et al. (2007). The Atmospheric Radiation Measurement Program cloud profiling radars: Second-generation sampling strategies, processing, and cloud data products. *Journal of Atmospheric and Oceanic Technology*, *24*(7), 1199–1214. https://doi.org/10.1175/JTECH2033.1

Kollias, P., Clothiaux, E. E., Ackerman, T. P., Albrecht, B. A., Widener, K. B., Moran, K. P., et al. (2016). Development and applications of ARM millimeter-wavelength cloud radars. In *The Atmospheric Radiation Measurement (ARM) Program: The First 20 Years*, *Meteorological Monographs* (Vol. 57, pp. 17.1–17.19). Boston, MA: American Meteorological Society. https://doi.org/10.1175/AMSMONOGRAPHS-D-15-0037.1

Korolev, A., & Isaac, G. (2003). Roundness and aspect ratio of particles in ice clouds. *Journal of the Atmospheric Sciences*, *60*(15), 1795–1808. https://doi.org/10.1175/1520-0469(2003)060%3C1795:RAAROP%3E2.0.CO;2

Korolev, A. V., Isaac, G. A., Cober, S. G., Strapp, J. W., & Hallett, J. (2003). Microphysical characterization of mixed-phase clouds. *Quarterly Journal of the Royal Meteorological Society*, *129*(587), 39–65. https://doi.org/10.1256/qj.01.204

Kumjian, M. R., & Lombardo, K. A. (2017). Insights into the evolving microphysical and kinematic structure of northeastern U.S. winter storms from dual-polarization Doppler radar. *Monthly Weather Review*, *145*(3), 1033–1061. https://doi.org/10.1175/MWR-D-15-0451.1

Kumjian, M. R., Mishra, S., Giangrande, S. E., Toto, T., Ryzhkov, A. V., & Bansemer, A. (2016). Polarimetric radar and aircraft observations of saggy bright bands during MC3E. *Journal of Geophysical Research: Atmospheres*, *121*, 3584–3607. https://doi.org/10.1002/2015JD024446

Kumjian, M. R., Rutledge, S. A., Rasmussen, R. M., Kennedy, P. C., & Dixon, M. (2014). High-resolution polarimetric radar observations of snow generating cells. *Journal of Applied Meteorology and Climatology*, *53*(6), 1636–1658. https://doi.org/10.1175/JAMC-D-13-0312.1

Kumjian, M. R., Ryzhkov, A. V., Reeves, H. D., & Schuur, T. J. (2013). Dual-polarization radar observations of hydrometeor refreezing in winter storms. *Journal of Applied Meteorology and Climatology*, *52*(11), 2549–2566. https://doi.org/10.1175/JAMC-D-12-0311.1

Lawson, R. P., & Zuidema, P. (2009). Aircraft microphysical and surface-based radar observations of summertime Arctic clouds. *Journal of the Atmospheric Sciences*, *66*, 3505–3529. https://doi.org/10.1175/2009JAS3177.1

Lebo, Z. J., Johnson, N. C., & Harrington, J. Y. (2008). Radiative influences on ice crystal and droplet growth within mixed–phase stratus clouds. *Journal of Geophysical Research*, *113*, D09203. https://doi.org/10.1029/2007JD009262

Leinonen, J., & Moisseev, D. (2015). What do triple-frequency radar signatures reveal about aggregate snowflakes? *Journal of Geophysical Research: Atmospheres*, *120*, 229–239. https://doi.org/10.1002/2014JD022072

Leinonen, J., & Szyrmer, W. (2015). Radar signatures of snowflake riming: A modeling study. *Earth and Space Science*, *2*(8), 346–358. https://doi.org/10.1002/2015EA000102

Liebe, H. J., Hufford, G. A., & Cotton, M. G. (1993). Propagation modeling of moist air and suspended water/ice particles at frequencies below 1000 GHz. In *Proc. AGARD Meeting Atmos. Propag. Effects Through Natural Man-Made Obscurants Visible MM-Wave Radiation*, 3/1-3/11.

Liljegren, J. C., Clothiaux, E. E., Mace, G. G., Kato, S., & Dong, X. (2001). A new retrieval for cloud liquid water path using a ground-based microwave radiometer and measurements of cloud temperature. *Journal of Geophysical Research*, *106*(D13), 14,485–14,500. https://doi.org/10.1029/2000JD900817

Lu, Y., Clothiaux, E. E., Aydin, K., Botta, G., & Verlinde, J. (2013). Modeling variability in dendritic ice crystal backscattering cross sections at millimeter wavelengths using a modified Rayleigh–Gans theory. *Journal of Quantitative Spectroscopy and Radiative Transfer*, *131*(2013), 95–104. https://doi.org/10.1016/j.jqsrt.2013.05.008

Lu, Y., Jiang, Z., Aydin, K., Verlinde, J., Clothiaux, E. E., & Botta, G. (2016). A polarimetric scattering database for non-spherical ice particles at microwave wavelengths. *Atmospheric Measurement Techniques*, *9*(10), 5119–5134. https://doi.org/10.5194/amt-9-5119-2016

Luke, E., Kollias, P., Johnson, K. L., & Clothiaux, E. E. (2008). A technique for the automatic detection of insect clutter in cloud radar returns. *Journal of Atmospheric and Oceanic Technology*, *25*, 1498–1513. https://doi.org/10.1175/2007JTECHA953.1

Luke, E., Kollias, P., & Shupe, M. D. (2010). Detection of supercooled liquid in mixed-phase clouds using radar Doppler spectra. *Journal of Geophysical Research*, *115*, D19201. https://doi.org/10.1029/2009JD012884

Magono, C., & Lee, C. W. (1966). Meteorological classification of natural snow crystals. *Journal of the Faculty of Science, Hokkaido University, Series VII*, *2*(4), 321–335.

Mather, J. H., & Voyles, J. W. (2013). The ARM Climate Research Facility: A review of structure and capabilities. *Bulletin of the American Meteorological Society*, *94*(3), 377–392. https://doi.org/10.1175/BAMS-D-11-00218.1

Matrosov, S. Y. (1991). Theoretical study of radar polarization parameters obtained from cirrus clouds. *Journal of the Atmospheric Sciences*, *48*, 1062–1070. https://doi.org/10.1175/1520-0469(1991)048%3C1062:TSORPP%3E2.0.CO;2

Matrosov, S. Y., Schmitt, C. G., Maahn, M., & de Boer, G. (2017). Atmospheric ice particle shape estimates from polarimetric radar measurements and in situ observations. *Journal of Atmospheric and Oceanic Technology*, *34*(12), 2569–2587. https://doi.org/10.1175/JTECH-D-17-0111.1

Moisseev, D., & Chandrasekar, V. (2007). Nonparametric estimation of raindrop size distributions from dual-polarization radar spectral observations. *Journal of Atmospheric and Oceanic Technology*, *24*, 1008–1018. https://doi.org/10.1175/JTECH2024.1

Moisseev, D. N., Lautaportti, S., Tyynela, J., & Lim, S. (2015). Dual-polarization radar signatures in snowstorms: Role of snowflake aggregation. *Journal of Geophysical Research*, *120*, 12,644–12,655. https://doi.org/10.1002/2015JD023884

Morrison, H., de Boer, G., Feingold, G., Harrington, J., Shupe, M. D., & Sulia, K. (2012). Resilience of persistent arctic mixed-phase clouds. *Nature Geoscience*, *5*(1), 11–17. https://doi.org/10.1038/NGEO1332

Myagkov, A., Seifert, P., Wandinger, U., Bühi, J., & Engelmann, R. (2016). Relationship between temperature and apparent shape of pristine ice crystals derived from polarimetric cloud radar observations during the ACCEPT campaign. *Atmospheric Measurement Techniques*, *9*, 3739–3754. https://doi.org/10.5194/amt-9-3739-2016

Orr, B. W., & Kropfli, R. (1999). A method for estimating particle fall velocities from vertically pointing Doppler radar. *Journal of Atmospheric and Oceanic Technology*, *16*(1), 29–37. https://doi.org/10.1175/1520-0426(1999)016%3C0029:AMFEPF%3E2.0.CO;2

Oue, M., Galletti, M., Verlinde, J., Ryzhkov, A., & Lu, Y. (2016). Use of X-band differential reflectivity measurements to study shallow Arctic mixed-phase clouds. *Journal of Applied Meteorology and Climatology*, *55*(2), 403–424. https://doi.org/10.1175/JAMC-D-15-0168.1

Oue, M., Kumjian, M. R., Lu, Y., Jiang, Z., Clothiaux, E. E., Verlinde, J., & Aydin, K. (2015). X-band polarimetric and Ka-band Doppler spectral radar observations of a graupel-producing Arctic mixed-phase cloud. *Journal of Applied Meteorology and Climatology*, *54*(6), 1335–1351. https://doi.org/10.1175/JAMC-D-14-0315.1

Oue, M., Kumjian, M. R., Lu, Y., Verlinde, J., Aydin, K., & Clothiaux, E. E. (2015). Linear depolarization ratios of columnar ice crystals in a deep precipitating system over the Arctic observed by zenith-pointing Ka-band Doppler radar. *Journal of Applied Meteorology and Climatology*, *54*(5), 1060–1068. https://doi.org/10.1175/JAMC-D-15-0012.1

Pfitzenmaier, L., Dufourmet, Y., Unal, C. M. H., & Russchenberg, H. W. J. (2017). Retrieving fall streaks within cloud systems using Doppler radar. *Journal of Atmospheric and Oceanic Technology*, *34*(4), 905–920. https://doi.org/10.1175/JTECH-D-16-0117.1

Protat, A., & Williams, C. R. (2011). The accuracy of radar estimates of ice terminal fall speed from vertically pointing Doppler radar measurements. *Journal of Applied Meteorology and Climatology*, *50*, 2120–2138. https://doi.org/10.1175/JAMC/-D-10-05031.1

Pruppacher, H. R., & Klett, J. D. (2010). *Microphysics of Clouds and Precipitation* (p. 975). Dordrecht Heidelberg London New York: Springer. https://doi.org/10.1007/978-0-306-48100-0

Rambukkange, M. P., Verlinde, J., Eloranta, E. W., Flynn, C. J., & Clothiaux, E. E. (2011). Using Doppler spectra to separate hydrometeor populations and analyze ice precipitation in multilayered mixed-phase clouds. *IEEE Geoscience and Remote Sensing Letters, IEEE*, *8*(1), 108–112. https://doi.org/10.1109/LGRS.2010.2052781

Reinking, R. F., Matrosov, S. Y., Bruintjes, R. T., & Martner, B. E. (1997). Identification of hydrometeors with elliptical and linear polarization K_a-band radar. *Journal of Applied Meteorology*, *36*(4), 322–339. https://doi.org/10.1175/1520-0450(1997)036%3C0322:IOHWEA%3E2.0.CO;2

Ryzhkov, A. V., Giangrande, S. E., Melnikov, V. M., & Schuur, T. J. (2005). Calibration issues of dual-polarization radar measurements. *Journal of Atmospheric and Oceanic Technology*, *22*(8), 1138–1155. https://doi.org/10.1175/JTECH1772.1

Ryzhkov, A. V., Zhang, P., Reeves, H. D., Kumjian, M. R., Tschallener, T., Trömel, S., & Simmer, C. (2016). Quasi-vertical profiles—A new way to look at polarimetric radar data. *Journal of Atmospheric and Oceanic Technology*, *33*(3), 551–562. https://doi.org/10.1175/JTECH-D-15-0020.1

Ryzhkov, A. V., Zrnić, D. S., & Gordon, B. A. (1998). Polarimetric method for ice water content determination. *Journal of Applied Meteorology*, *37*(2), 125–134. https://doi.org/10.1175/1520-0450(1998)037%3C0125:PMFIWC%3E2.0.CO;2

Schneebeli, M., Dawes, N., Lehning, M., & Berne, A. (2013). High-resolution vertical profiles of X-band polarimetric radar observables during snowfall in the Swiss Alps. *Journal of Applied Meteorology and Climatology*, *52*(2), 378–394. https://doi.org/10.1175/JAMC-D-12-015.1

Schrom, R. S., & Kumjian, M. R. (2016). Connecting microphysical processes in Colorado winter storms with vertical profiles of radar observations. *Journal of Applied Meteorology and Climatology*, *55*(8), 1771–1787. https://doi.org/10.1175/JAMC-D-15-0338.1

Schrom, R. S., Kumjian, M. R., & Lu, Y. (2015). Polarimetric radar signatures of dendritic growth zones within Colorado winter storms. *Journal of Applied Meteorology and Climatology*, *54*(12), 2365–2388. https://doi.org/10.1175/JAMC-D-15-0004.1

Seliga, T. A., Bringi, V. N. & Al-Khatib, H. H. (1981). A preliminary study of comparative measurements of rainfall rate using the differential reflectivity radar technique and a raingage network. *Journal of Applied Meteorology*, *20*, 1362–1368. https://doi.org/10.1175/1520-0450(1981)020<1362:APSOCM>2.0.CO;2

Shupe, M., Kollias, P., Matrosov, S. Y., & Schneider, T. L. (2004). Deriving mixed-phase cloud properties from Doppler radar spectra. *Journal of Atmospheric and Oceanic Technology*, *21*, 660–670. https://doi.org/10.1175/1520-0426(2004)021%3C0660:DMCPFD%3E2.0.CO;2

Shupe, M. D. (2011). Clouds at Arctic atmospheric observatories. Part II: Thermodynamic phase characteristics. *Journal of Atmospheric and Oceanic Technology*, *50*(3), 645–661. https://doi.org/10.1175/2010JAMC2468.1

Shupe, M. D., Daniel, J. S., de Boer, G., Eloranta, E. W., Kollias, P., Luke, E. P., et al. (2008). A focus on mixed-phase clouds: The status of ground-based observational methods. *Bulletin of the American Meteorological Society*, *89*, 1549–1562. https://doi.org/10.1175/2008BAMS2378.1

Sinclair, V. A., Moisseev, D., & von Lerber, A. (2016). How dual-polarization radar observations can be used to verify model representation of secondary ice. *Journal of Geophysical Research: Atmospheres*, *121*, 10,954–10,970. https://doi.org/10.1002/2016JD025381

Straka, J., Zrnic, D. S., & Ryzhkov, A. V. (2000). Bulk hydrometeor classification and quantification using polarimetric radar data: Synthesis of relations. *Journal of Applied Meteorology*, *39*(8), 1341–1372. https://doi.org/10.1175/1520-0450(2000)039%3C1341:BHCAQU%3E2.0.CO;2

Straka, J. M., & Zrnić, D. S. (1993). An algorithm to deduce hydrometeor types and contents from multiparameter radar data. In *Preprints, 26th Conf. on Radar Meteorology* (pp. 513–516). Norman, OK: American Meteorological Society.

Tan, I., Storelvmo, T., & Zelinka, M. D. (2016). Observational constraints on mixed-phase clouds imply higher climate sensitivity. *Science*, *352*(6282), 224–227. https://doi.org/10.1126/science.aad5300

Thompson, E. J., Rutledge, S. A., Dolan, B., Chandrasekar, V., & Cheong, B. L. (2014). A dual-polarization radar hydrometeor classification algorithm for winter precipitation. *Journal of Atmospheric and Oceanic Technology*, *31*(7), 1457–1481. https://doi.org/10.1175/JTECH-D-13-00119.1

Tridon, F., Battaglia, A., & Kollias, P. (2013). Disentangling Mie and attenuation effects in rain using a Ka/W dual-wavelength Doppler spectral ratio technique. *Geophysical Research Letters*, *40*, 5548–5552. https://doi.org/10.1002/2013GL057454

Tyynelä, J., Leinonen, J., Moisseev, D., & Nousiainen, T. (2011). Radar backscattering From snowflakes: Comparison of fractal, aggregate and soft-spheroid models. *Journal of Atmospheric and Oceanic Technology*, *28*(11), 1365–1372. https://doi.org/10.1175/JTECH-D-11-00004

Unal, C. (2015). High-resolution raindrop size distribution retrieval based on the Doppler spectrum in the case of slant profiling radar. *Journal of Atmospheric and Oceanic Technology*, *32*, 1191–1208. https://doi.org/10.1175/JTECH-D-13-00225.1

Verlinde, J., Rambukkange, M. P., Clothiaux, E. E., McFarquhar, G. M., & Eloranta, E. W. (2013). Arctic multilayered, mixed-phase cloud processes revealed in millimeter-wave cloud radar Doppler spectra. *Journal of Geophysical Research: Atmospheres*, *118*, 13,199–13,213. https://doi.org/10.1002/2013JD020183

Vivekanandan, J., Bringi, V., Hagen, M., & Meischner, P. (1994). Polarimetric radar studies of atmospheric ice particles. *IEEE Transactions on Geoscience and Remote Sensing*, *32*(1), 1–10. https://doi.org/10.1109/36.285183

Westbrook, C. D. (2014). Rayleigh scattering by hexagonal ice crystals and the interpretation of dual-polarization radar measurements. *Quarterly Journal of the Royal Meteorological Society*, *140*(683), 2090–2096. https://doi.org/10.1002/qj.2262

Williams, E., Smalley, D., Donovan, M., Hallowell, R., Hood, K., Bennett, B., et al. (2015). Measurements of differential reflectivity in snowstorms and warm season stratiform systems. *Journal of Applied Meteorology and Climatology*, *54*(3), 573–595. https://doi.org/10.1175/JAMC-D-14-0020.1

Xu, Y.-L. (1995). Electromagnetic scattering by an aggregate of spheres. *Applied Optics*, *34*(21), 4573–4588. https://doi.org/10.1364/AO.34.004573

Yu, G., Verlinde, J., Clothiaux, E. E., & Chen, Y.-S. (2014). Mixed-phase cloud phase partitioning using millimeter wavelength cloud radar Doppler velocity spectra. *Journal of Geophysical Research: Atmospheres*, *119*, 7556–7576. https://doi.org/10.1002/2013JD021182

Zawadzki, I., Fabry, F., & Szyrmer, W. (2001). Observations of supercooled water and secondary ice generation by a vertically pointing X-band Doppler radar. *Atmospheric Research*, *59-60*, 343–359. https://doi.org/10.1016/S0169-8095(01)00124-7

Zhang, D., Wang, Z., & Liu, D. (2010). A global view of midlevel liquid-layer topped stratiform cloud distribution and phase partition from CALIPSO and CloudSat measurements. *Journal of Geophysical Research*, *115*, D00H13. https://doi.org/10.1029/2009JD012143